Forschungszentrum Karlsruhe
in der Helmholtz-Gemeinschaft

Wissenschaftliche Berichte
FZKA 7268

Application of the SVECHA/QUENCH Code to the Simulation of the Bundle Test QUENCH-10

A. V. Palagin

Institut für Materialforschung
Programm Nukleare Sicherheitsforschung

Januar 2007

Forschungszentrum Karlsruhe

in der Helmholtz-Gemeinschaft

Wissenschaftliche Berichte

FZKA 7268

Application of the SVECHA/QUENCH Code to the Simulation of the Bundle Test QUENCH-10

A.V. Palagin *

Institut für Materialforschung

Programm Nukleare Sicherheitsforschung

* European Commission, Joint Research Centre -
Institute for Transuranium Elements, Germany

Forschungszentrum Karlsruhe GmbH, Karlsruhe
2007

Forschungszentrum Karlsruhe GmbH
Postfach 3640, 76021 Karlsruhe

Mitglied der Hermann von Helmholtz-Gemeinschaft
Deutscher Forschungszentren (HGF)

ISSN 0947-8620

urn:nbn:de:0005-072689

Zusammenfassung

Anwendung des Codes SVECHA/QUENCH für die Modellierung des Bündelversuches QUENCH-10

Für die Modellierung des Bündelversuches QUENCH-10 wurde der Code SVECHA/QUENCH mit dem sog. Effektiv-Kanal-Model angewendet. Dieses Model wurde bereits für die Modellierung der früheren QUENCH-Versuche verwendet. Die an beheizten Stäben gemessenen Temperaturen wurden bearbeitet, geglättet und dann als Randbedingungen für den Zentralstab angewendet. Alle Versuchsphasen (Aufheizen, Voroxidation, Übergang, Lufteinbruch, Wasserabschreckung) wurden analysiert. Da das Modell für die Wechselwirkung zwischen Zirkonium und Stickstoff noch nicht entwickelt und in den SVECHA-Code eingeführt ist, wird nur die Wechselwirkung zwischen dem Zr-Hüllrohr und dem Sauerstoff als eine Komponente der Luft beschrieben. Die Berechnungen geben die zeitliche Temperaturentwicklung des Zentralstabes an unterschiedlichen Bündelhöhen für die ganze Dauer des Versuches, auch während der Abschreckphase, adäquat wieder. Die berechnete axiale Oxidschichtverteilung entspricht gut der aus den gemessenen Werten. Die berechnete Wasserstoffproduktionsrate gibt sehr gut die zeitliche Abhängigkeit der gemessenen Werte wieder, die absoluten Werte hingegen liegen im Vergleich zu den Messwerten niedriger.

Abstract

SVECHA/QUENCH code was applied to the simulation of the QUENCH bundle test Q-10. The simulation was performed within the framework of the 'effective channel approach', which has been developed and applied to the simulation of a number of QUENCH bundle tests earlier. The experimentally measured temperatures of the heated rods were processed, smoothed and then used as boundary conditions for the central rod. All the stages of the Q-10 test (heatup, preoxidation, transient, air ingression, water quenching) were considered. Since the specific model of zirconium-nitrogen physical-chemical interaction has not been yet developed and implemented in the S/Q code, only oxygen interaction with Zr cladding as one of the air components was described. The calculations adequately reproduce temperature evolution of the central rod at different elevations during the whole test duration including quenching phase. The calculated oxide axial profile agrees quite well with the experimental data. The calculated hydrogen production rate well reproduces time dependence of the experimentally measured one, but its absolute value appears to be underestimated.

CONTENTS

LIST OF TABLES

LIST OF Figures

1 Introduction

In the present work the QUENCH bundle test Q-10 was simulated by the SVECHA/QUENCH (S/Q) code [1-3]. Within the framework of the S/Q code the main physical phenomena occurring during quenching of fuel rods are considered.

Zirconium oxidation leads to the heat release and hydrogen generation and affects the mechanical properties of the cladding. High cooling rates in the course of quenching sustain non-equilibrium conditions at the interface boundaries of the cladding layers and lead to the appearance of a temperature gradient across the cladding. The **Oxidation model** based on the partial derivative equations for the multi-layer oxygen diffusion problem describes the oxidation kinetics under these conditions.

Zircaloy can dissolve large amounts of hydrogen even at high temperatures. Therefore, Zircaloy can act as a sink or source of hydrogen, depending on the environmental conditions. In this way the hydrogen solubility of the cladding material can alter the hydrogen source term. The **Hydrogen Absorption model** considers cladding interactions with hydrogen/steam mixtures and hydrogen absorption by Zircaloy. The model was tightly coupled with the Oxidation model and the two models were implemented in the S/Q code as a combined module.

Cold water injection in the hot core gives rise to the high temperature gradients in the oxidized Zircaloy cladding and initiates oxide layer cracking. The axial temperature gradient at the quench front elevation as well as phase transitions in the cladding materials on cool-down (or heat-up in the case of possible temperature escalation) can lead to the through-wall crack formation and possible fragmentation of the oxidized Zircaloy cladding. The **Mechanical Deformation model** accounts for the effect of the temperature gradients, $\beta \rightarrow \alpha$ (Zry) and tetragonal-to-monoclinic (ZrO_2) phase transformations on the stress state of the oxidized cladding under quenching conditions and correctly predicts the rod specimen failure modes (cracking, spalling, breaching) observed in the quench tests.

The description of the heat exchange process requires simultaneous solution of two problems: (i) heat conduction problem inside the solid body (fuel rod) and (ii) heat convection problem in the surrounding two-phase water-steam media. For the solution of the first problem in the axially non-uniform multi-layer cylindrical structure (fuel pellets/gap/cladding) the **Heat Conduction module** was developed. This module is based on the 2-D finite differences numerical scheme with adaptive grid. **Thermal-Hydraulic module** elaborated for the description of the heat convection process accounts for the heat exchange and non-stationary motion of different water-steam regions.

The heat exchange in the core determines the temperature of the rod surface and thus the oxidation kinetics, hydrogen generation and mechanical deformations of the cladding. The heat released due to Zr oxidation considerably affects the heat exchange, especially at high temperatures. The mechanical behaviour of the cladding determines cladding rupture that provides direct access of oxygen to fresh (non-oxidized) metal surfaces and thus intensification of oxidation and hydrogen production rates.

Therefore, the profound mutual influence of the studied phenomena determines complex behaviour of the cladding system during rod quenching. For the adequate description of this process the self-consistent coupling of the Oxidation, Hydrogen Absorption, Mechanical Deformation, Heat Conduction and Thermal-Hydraulic modules within the framework of the S/Q code was performed.

The S/Q code was elaborated on the basis of the FZK single rod quenching tests in close cooperation with the FZK QUENCH team and was intensively verified against these tests.

The present simulation of the QUENCH bundle test by the S/Q code was performed using the 'effective channel' approach [4-8].

Since the central rod of the bundle is not heated, its temperature evolution in the course of reflooding experiment is completely determined by thermal-hydraulic boundary conditions: temperatures of the surrounding heated rods and shroud and characteristics of the coolant flow (boiling regime, flooding rate, gas phase velocity and composition, etc.). In the case of full-scale simulation of the bundle test the temperatures of the heated rods and shroud are calculated by specifying the electric power time evolution and thus, the boundary conditions for the central rod are determined by the code. At the same time, there exists another possibility to determine the boundary conditions for the central rod: instead of calculation, the temperatures of the heated rods and shroud may be taken from the experiment.

From the viewpoint of the solution of the heat conduction problem inside the central rod both ways are equivalent. Specification of the boundary conditions on the basis of the experimentally measured temperatures even has certain advantages as it describes the thermal regime around the central rod very close to that in the experiment.

Within the framework of the S/Q code the thermal boundary conditions for the central rod may be predetermined by specifying the temperatures of the "effective channel" inner wall on the basis of experimentally measured temperatures. The inner surface of the effective channel represents the surfaces of the heated rods surrounding the central rod.

The heat exchange between the central rod and the effective channel is affected via radiation and heat transfer through the water-gas media filling the channel. The thermal-hydraulic characteristics of the effective channel (cross-section, hydraulic diameter) are determined on the basis of geometrical parameters of the bundle (total cross-section, number of rods and their diameters).

The appropriate determination of the effective channel parameters and temperature evolution makes it possible to reproduce very closely the experimental thermal conditions around the central rod. Since the S/Q code uses fine adaptive meshing and accounts for all the details of the heat conduction process (layers thickness variation, different thermal properties of different layers, etc. [1, 3]) it allows a correct solution of the temperature problem inside the rod on the basis of such boundary conditions.

The correct reproduction of the rod temperature evolution in its turn allows a detailed description of cladding mechanical deformation, oxidation and hydrogen absorption processes dur-

ing reflooding, which were treated by the S/Q in the most advanced mechanistic approach. In the present work all the stages of the Q-10 test [9, 10] (heatup, preoxidation, transient, air ingression, water quenching) were properly analysed by the S/Q code. A number of important parameters (rod temperature variation, oxide layer thickness, hydrogen production rate, etc.) were calculated and compared with the experimentally measured ones.

Within the framework of the effective channel approach the experimentally measured temperatures at all the elevations (TFS and TSH thermocouples data) were analyzed and smoothed. At high elevations the TFS data were used as the basis for the averaged temperature. At the elevations from 1050 mm to 750 mm the TFS data were used up to the moment of corresponding TC failure, then TSH and TCRC/TIT data were taken as such basis. At lower elevations (below 550 mm) only TFS data were applied.

The calculated 'averaged temperature field' describing temperature evolution around central rod was used in the S/Q code input files for the simulation of the quench bundle tests Q-10. The calculated oxide thickness axial profile was compared with the experimentally measured one at three time moments corresponding to the withdrawn of the corner rods B and D and at the end of the test. The calculated hydrogen production rate was compared with the experimental data.

2 Processing of the Q-10 bundle test temperature data

During the QUENCH-10 test [9, 10] the temperature was continuously measured at different locations of the bundle. 26 thermocouples were attached to the cladding of the heated rods at 15 different elevations between -250 mm and 1350 mm; 2 thermocouples were inserted in the centres of two corner rods at 850 and 950 mm elevations; 2 thermocouples were located between cladding and pellets inside central rod at 550 and 350 mm; 2 thermocouples were located in the centre of the central rod at 950 and 850 mm. The TCs data were processed by the FZK experimental team, incorrect data were deleted and now these data are available in the electronic format. Table 1 presents the TCs designations, corresponding rod numbers and elevations.

23 thermocouples were located at the shroud outer surface at 12 different elevations between -250 mm and 1250 mm. Since the TCs were protected by the shroud wall from direct contact with steam, all of them survived throughout the test. Table 2 presents designations and elevations of the shroud thermocouples, available in the electronic format.

The above TCs data were used for the simulation of the effective channel internal surface. The numerical procedure of the rod TCs data recalculation includes smoothening, averaging and interpolation. These operations are described below.

1. In Figs. 1-2 the original TC readings of TFS2/17 and TFS5/17 thermocouples as well as the calculated averaged temperature (**TFS_17**) at the elevation 1350 mm are presented. The averaged temperature was calculated as arithmetic mean of the smoothed TFS2/17 and TFS5/17 data sets.

	Channel	TC	Elevation
1	KAN: 04	TFS2/17 F	1350 mm
2	KAN: 49	TFS5/17	1350 mm
3	KAN: 37	TFS3/16	1250 mm
4	KAN: 48	TFS5/16	1250 mm
5	KAN: 03	TFS2/15	1150 mm
6	KAN: 47	TFS5/15	1150 mm
7	KAN: 09	TFS3/14	1050 mm
8	KAN: 16	TFS5/14	1050 mm
9	KAN: 08	TFS3/13	950 mm
10	KAN: 11	TFS4/13	950 mm
11	KAN: 51	TFS2/11	750 mm
12	KAN: 06	TFS5/11	750 mm
13	KAN: 39	TFS2/9	550 mm
14	KAN: 34	TFS4/9	550 mm
15	KAN: 38	TFS5/9	550 mm
16	KAN: 43	TFS3/8	450 mm
17	KAN: 42	TFS5/8	450 mm
18	KAN: 23	TFS2/7	350 mm
19	KAN: 82	TFS5/7	350 mm
20	KAN: 76	TFS2/6 F	250 mm
21	KAN: 81	TFS5/6	250 mm
22	KAN: 22	TFS 2/5	150 mm
23	KAN: 78	TFS 5/4/0 F	50 mm
24	KAN: 79	TFS 5/4/180	50 mm
25	KAN: 74	TFS 2/3	-50 mm
26	KAN: 72	TFS 2/1 F	-250 mm
27	KAN: 32	TIT A/13	950 mm
28	KAN: 33	TCRC 13	950 mm
29	KAN: 40	TIT C/12	850 mm
30	KAN: 50	TCRC 12	850 mm
31	KAN: 77	TCR 9	550 mm
32	KAN: 75	TCR 7	350 mm

Table 1. Locations of the TCs used for the Fuel Rod Simulators temperature measurement in the QUENCH-10 bundle test.

	Channel	TC	Elevation
1	KAN: 67	TSH 16/0 I	1250 mm
2	KAN: 17	TSH 16/180 I	1250 mm
3	KAN: 66	TSH 15/0 I	1150 mm
4	KAN: 05	TSH 15/180 I	1150 mm
5	KAN: 19	TSH 14/90 I	1050 mm
6	KAN: 53	TSH 14/270 I	1050 mm
7	KAN: 52	TSH 13/270 I	950 mm
8	KAN: 21	TSH 12/0 I	850 mm
9	KAN: 55	TSH 12/180 I	850 mm
10	KAN: 20	TSH 11/0 I	750 mm
11	KAN: 54	TSH 11/180 I	750 mm
12	KAN: 15	TSH 10/90	550 mm
13	KAN: 02	TSH 9/0	550 mm
14	KAN: 35	TSH 9/90	550 mm
15	KAN: 36	TSH 9/270	550 mm
16	KAN: 90	TSH 7/0	350 mm
17	KAN: 86	TSH 7/180	350 mm
18	KAN: 89	TSH 4/0	50 mm
19	KAN: 87	TSH 4/90	50 mm
20	KAN: 85	TSH 4/180	50 mm
21	KAN: 83	TSH 4/270	50 mm
22	KAN: 84	TSH 3/180	- 50 mm
23	KAN: 88	TSH 1/0	-250 mm

Table 2. Locations of the TCs used for the shroud temperature measurement in the QUENCH-10 bundle test

2. In Figs. 3-4 the original TC readings of TFS3/16 and TFS5/16 thermocouples as well as the calculated averaged temperature (**TFS_16**) at the elevation 1250 mm are presented. Starting from 11646 sec. (beginning of sharp temperature rise) the data of TFS3/16 thermocouple are considered as erroneous due to TC failure and only TFS5/16 data were used for the evaluation of the averaged temperature.

3. In Figs. 5-6 the original TC readings of TFS2/15 and TFS5/15 thermocouples as well as the calculated averaged temperature (**TFS_15**) at the elevation 1150 mm are presented. Up to the moment of TFS2/15 drop down (due to possible problems with the

rod surface contact, 6914 sec.) the averaged temperature was calculated as arithmetic mean of the smoothed TFS2/15 and TFS5/15 data sets. After this moment only TFS5/15 data were used as the basis for **TFS_15** with the assumption that the difference between **TFS_15** and TFS5/15 is constant and equal to the value of this difference at the moment of TFS2/15 failure (50.1 K).

4. In Figs. 7-8 the original TC readings of TFS3/14 and TFS5/14 thermocouples, TSH14/90_I and TSH14/270_I thermocouples at the elevation 1050 mm as well as the calculated averaged temperature (**TFS_14**) are presented. Here the averaged temperature TFS_14 was calculated as arithmetic mean of the smoothed TFS3/14 and TFS5/14 data sets up to the moment of TFS3/14 inadequate behaviour beginning (5958 sec.). After this moment up to the 6801 sec., when the inadequate behaviour of TFS5/14 began only TFS5/14 data were used as the basis for **TFS_14** with the assumption that the difference between **TFS_14** and TFS5/14 is constant and equal to the value of this difference at the moment of TFS3/14 failure (7.1 K).

5. The conclusion about the inadequacy of TFS3/14 and TFS5/14 thermocouples was made on the basis of the comparison of the TFS type TCs located at the surface of the heated rods and the TSH type TCs located at the shroud outer surface and thus protected from oxidation in steam/argon atmosphere. After indicated above time moments the rod TCs show irregular behaviour, sharp oscillations and drops with general tendency to decreasing of the temperature, whereas two shroud TCs demonstrate well-correlated and stable behaviour at the preoxidation, transient and air ingress phases of the test. That is why after the failure of both TFS thermocouples we used TSH data in order to represent the temperature evolution at 1050 mm elevation.

6. After 6801 sec. the arithmetic mean of the smoothed TSH14/90_I and TSH14/270_I data sets was used as the basis for **TFS_14** with the assumption that the difference between **TFS_14** and averaged TSH/14 data is equal to the value of this difference at the moment of TFS3/14 failure (265 K) during preoxidation and transient phases and gradually decreased during air ingress phase. Lack of rod TCs data introduces some uncertainty in the evaluated temperature evolution at the considered elevation. However, comparison of the calculated and measured oxide thickness (see below, subsec 4.2) at the elevation 1050 mm implicitly confirms the correctness of the evaluated temperature evolution.

7. At the elevation 950 mm (Fig. 9) the TFS3/13 and TFS4/13 thermocouples failed long before transient phase. The smoothed TITA/13 (corner rod thermocouple) data set was considered as the basis for the evaluation of the averaged temperature **TFS_13** at this elevation.

8. At the elevation 850 mm (Fig. 10) the averaged temperature **TFS_12** was calculated as arithmetic mean of the smoothed TITC/12 and TCRC 12 data sets.

9. At the elevation 750 mm (Figs. 11) the average temperature **TFS_11** was determined as arithmetic mean of smoothed TFS2/11 and TFS5/11 up to the moment of TFS2/11 inadequate behaviour beginning (7103 sec.). After this moment up to the 9450 sec.,

when the inadequate behaviour of TFS5/11 began only TFS5/11 data were used as the basis for **TFS_11** with the assumption that the difference between **TFS_11** and TFS5/11 is constant and equal to the value of this difference at the moment of TFS2/11 failure (42.5 K). After 9450 sec. the data sets of shroud thermocouples TSH11/0_I and TSH11/180_I were used as the basis for the averaged temperature **TFS_11** at the elevation 750 mm.

At the elevations from 650 mm to -250 mm all the TFS thermocouples survived throughout the test. That is why the average temperatures at these elevations were determined as arithmetic mean of the corresponding smoothed TFS curves.

The calculated average temperature curves representing temperature evolution of the bundle at 17 elevations from 1350 mm to -250 mm are given in Figs. 12-14. These curves were used as the boundary conditions for the effective channel walls in the S/Q code simulation of the Q-10 test described below.

3 Q-10 bundle test simulation

3.1 Effective channel parameters determination

The parameters of the effective channel in the present calculation were determined in the same way as for the previous QUENCH bundle tests simulation [4-8].

The following bundle parameters were used for the channel determination:

Shroud inner diameter	D_{sh} = 80.0 mm;
Rod outside diameter	D_r = 10.75 mm;
Instrumentation tube diameter	D_t = 6.0 mm;
Number of rods	N_r = 21;
Number of corner rods	N_t = 4.

The total bundle cross-section is given by the expression:

$$A_{tot} = \frac{1}{4}\pi \cdot D_{sh}^2 - N_r \cdot \frac{1}{4}\pi \cdot D_r^2 - N_t \cdot \frac{1}{4}\pi \cdot D_t^2 . \quad (1)$$

The value of A_{tot} is equal to 30.07 cm^2.

The value of the channel cross-section per one rod is equal to

$$A_{eff} = \frac{A_{tot}}{N_r + N_t} = 1.203\,\mathrm{cm}^2 . \quad (2)$$

The effective channel inner radius is connected with the value of A_{eff} by:

$$\pi R_{eff}^2 - \frac{1}{4}\pi D_r^2 = A_{eff} \;\Rightarrow\; R_{eff} = \sqrt{\frac{A_{eff}}{\pi} + \frac{D_r^2}{4}} = 8.197\,\mathrm{mm} . \quad (3)$$

3.2 Test simulation specifications

The calculated average temperature curves representing temperature evolution of the bundle at 17 elevations from 1350 mm to -250 mm are given in Figs. 12-14. These curves were used as the boundary conditions for the effective channel walls in the S/Q code simulation of the Q-10 test described below

The average temperature field around the central rod, determined in the Section 2 was used as boundary conditions for the heat exchange problem.

On the basis of the effective channel parameters specified in the Subsection 3.1, the argon and steam mass flows at all the test phases were determined. By definition, inlet gas flow in the effective channel is connected with the total inlet gas flow by:

$$J_{eff} = J_{tot}\frac{A_{eff}}{A_{tot}} . \quad (4)$$

The value of argon total inlet flow rate was specified to be constant and equal to 3.0 g/s. The value of steam total flow rate was taken to be constant and equal to 3.0 g/s up to the moment of 11626 sec. and then replaced by of air flow reaching 1 g/s at 11658 sec.

At 13393 sec. the air ingress was stopped and water flooding began with flow rate of $J_{flood} = 50$ g/s. The estimated kinematical velocity of water level motion (without accounting for evaporation and two-phase water-steam regions formation) is given by

$$U_{flood} = \frac{J_{flood}}{A_{tot}} = 1.66 \text{ cm/s.} \quad (5)$$

Time step throughout the test values were:

1.0 s up to 12794 s,

0.1 s up to 13570 s,

1.0 s up to the end of the calculation.

The bundle nodalization is characterised by the following values:

Heat conduction module

- The total nodes number in the radial direction: 35
- Pellet nodes number in the radial direction: 21
- External layer (oxide) nodes number: 7
- Total nodes number in the vertical direction: 197

The vertical grid used in the heat conduction module is adaptive one, with maximum density in the region of the maximum temperature axial gradients.

Total number of meshes used by oxidation, mechanical deformation and hydrogen absorption modules was 98. The total central rod length considered was 1975 mm – from the upper point 1500 mm (adjacent to the Al_2O_3 plate thermal shield) to the lower point -475 mm (adjacent to the lower SS plate).

3.3 Air thermo-physical properties

Up to the present work thermal-physical properties of air were not described by the S/Q code. Necessary properties of nitrogen were implemented in the code material properties data base in the course of the S/Q code preparation for the Q-10 bundle test simulation. The argon-air mixture was then described as the mixture of argon, nitrogen and oxygen within the framework of the S/Q code gas mixture model [11].

3.3.1 Nitrogen thermo-physical properties

1. Molar mass $\mu_{N_2} = 0.028$ [kg]

2. Heat capacity [J/(kg·K)] [12]:

$$C_{N_2}(T) = \frac{1}{28.0 \cdot 10^{-3}} \cdot \left(26.4 + 7.913 \cdot 10^{-3} \cdot T - 1.44 \cdot 10^{-6} \cdot T^2\right). \quad (6)$$

3. Thermal conductivity [13]:

Temperature [K]	Thermal conductivity, 10^{-3} [W/(m·K)]
300	26.1
400	32.7
600	44.8
800	56.4
1000	67.6
1500	93.1
2000	115.0
2500	135.5

Table 3. Thermal conductivity of Nitrogen

4. Viscosity [13]:

Temperature [K]	Viscosity, 10^{-6} [kg/(m·s)]
300	17.9
400	22.1
500	25.9
600	29.3
800	35.2
1000	40.4
1500	54.4
2000	66.8
2200	71.3

Table 4. Viscosity of Nitrogen

3.3.2 Gas mixture properties

In the channel gas model the values of components mass concentrations (ratio of the component mass to the total mixture mass in a volume element) c_i are used in the mass balance equations. The sum of the mass concentrations is equal to unit:

$$\sum_i c_i = 1. \tag{7}$$

In the determination of the gas mixture properties the values of the molar fractions are also used:

$$x_i = \frac{c_i}{\mu_i}\left[\sum_i \frac{c_i}{\mu_i}\right]^{-1}. \tag{8}$$

Here μ_i are the molar masses of the mixture components. The density of the gas mixture [kg/m^3] is given by:

$$\rho(P,T) = \frac{P}{RT}\left[\sum_i \frac{c_i}{\mu_i}\right]^{-1}. \tag{9}$$

Heat capacity of the gas mixture [J/(kg·K)] is determined by:

$$C(P,T) = \sum_i C_i(P,T)\cdot c_i. \tag{10}$$

Thermal conductivity of the gas mixture [W/(m·K)] is determined by the following semi-empirical relation [12, 14]:

$$\lambda(T) = \sum_i \frac{x_i \lambda_i(T)}{x_i + S(T)}, \tag{11}$$

where

$$S(T) = \sum_{j\neq i} x_j \psi_{ij}(T), \tag{12}$$

$$\psi_{ij}(T) = \phi_{ij}(T)\left[1 + 2.41\frac{(\mu_i - \mu_j)(\mu_i - 0.142\mu_j)}{(\mu_i + \mu_j)^2}\right], \tag{13}$$

$$\phi_{ij}(T) = \frac{\left[1 + (\lambda_i(T)/\lambda_j(T))^{0.5}(\mu_i/\mu_j)^{0.25}\right]^2}{2\sqrt{2}(1+\mu_i/\mu_j)^{0.5}}, \tag{14}$$

Viscosity of the gas mixture [kg/(m·s)] is determined by [12, 15]:

$$\eta(T) = \sum_i \frac{x_i \eta_i(T)}{\sum_j x_j \varphi_{ij}(T)}, \tag{15}$$

where

$$\varphi_{ij}(T) = \frac{\left[1 + (\eta_i(T)/\eta_j(T))^{0.5}(\mu_i/\mu_j)^{0.25}\right]^2}{2\sqrt{2}(1+\mu_i/\mu_j)^{0.5}}, \tag{16}$$

3.4 Accounting for the Zirconium-air interaction effects

Since the specific model of zirconium-nitrogen physical-chemical interaction has not been yet developed and implemented in the S/Q code, only oxygen interaction with Zr cladding as one of the air components was described in the present work. With respect to the heat effects of zirconium-air interaction such approach is quite justified since, according to the experimental results, nitrogen uptake during air ingress phase of the test was about 10 times lower in comparison with oxygen uptake (8 and 84 g, respectively [9]). As for the cladding mechanical degradation and zirconium nitrides formation in the air atmosphere, the description of these phenomena requires development of the corresponding model.

The difference of the heat effects of Zr cladding oxidation in pure oxygen and steam is due to the fact that in the case of steam additional energy is needed for water molecule dissociation. That is why heat effect of Zr oxidation in pure oxygen is higher by the heat of water dissociation reaction in comparison with oxidation in steam. Standard heat of water dissociation reaction (per 1 mole of water)

$$H_2O \rightarrow H_2 + \frac{1}{2}O_2, \tag{17}$$

is given by [16]:

$$\frac{\Delta G^0_{H_2O}}{R_g T} = -6.61 + \frac{29600}{T}, \tag{18}$$

$R_g = 8.314510$ (J/mol·K) - universal gas constant.

In the temperature range of interest heat effect of Zr oxidation in pure oxygen appears to be 500-600 kJ per mole of atomic oxygen, i.e. approximately 2 times higher than that of oxidation in steam. This effect was accounted for by the S/Q code at the air ingress phase of Q-10 test simulation.

4 Simulation results

4.1 Calculated temperatures

In this subsection the calculated temperature evolution curves at the different elevations of the central rod are presented.

At the elevations above 950 mm the thermocouples located at the heated rods outer surface survived throughout the test (elevations 1350, 1250, 1150 mm) or at least during the main part of the test (1050 mm). So, the calculated temperature evolution of the central rod *outer surface* can be compared with that of the heated rods.

In Fig. 15 the experimentally measured temperatures at the elevation 1350 mm by TFS2/17 and TFS5/17 thermocouples as well as the calculated temperature evolution of the central rod outer surface at this elevation are presented.

In Fig. 16-18 the analogous comparison between the experimentally measured temperatures at the elevations 1250, 1150 and 1050 mm and the calculated temperature evolution of the central rod outer surface at these elevations is given.

At the elevation 950 mm the thermocouples located at the heated rods outer surface failed long before transient phase. At the elevation 850 mm no outer surface TCs were used. At these elevations the calculated temperature evolution of the central rod *pellet centre* can be compared with corresponding experimental data (readings of TCRC 13 and TCRC 12 thermocouples located in the central rod pellet centre as well as TIT A/13 and TIT C/12 located in the centre of two corner rods).

In Fig. 19 the experimentally measured temperatures at the elevation 950 mm by TCRC 13 and TIT A/13 thermocouples as well as the calculated temperature evolution of the central rod pellet centre at this elevation are presented.

In Fig. 20 the analogous comparison between the experimentally measured temperatures at the elevations 850 mm and the calculated temperature evolution of the central rod pellet centre at these elevations is given.

In Fig. 21 the experimentally measured temperatures at the elevation 750 mm by TFS2/11 and TFS5/11 thermocouples; by shroud thermocouples TSH11/0_I and TSH11/180_I as well as the calculated temperature evolution of the central rod outer surface at this elevation are presented.

The presented hottest part of the bundle (elevations from 1350 to 750 mm) is of the main interest with respect to oxidation and hydrogen production in the Q-10 test. At the elevation 650 mm no thermocouples located at the heated or central rod were used. Lower part of the bundle (550 mm and below) had relatively low temperature during the test and practically did not contribute to the oxidation and hydrogen production.

Calculated temperature evolution curves at the above elevations generally show good correlation with the experimentally measured ones during preoxidation, transient and air ingress phases of the test. All the characteristic bends of different test phases were properly reproduced by the calculations. At the same time, calculated temperatures are generally lower than the experimentally measured ones.

In Fig. 22-24 the experimentally measured temperatures of the rod outer surface at the elevations 1350, 1250 and 1150 mm and calculated temperature evolutions at these elevations at the quenching phase of the test (13350-13600 sec.) are presented. At the elevation 1050 mm the heated rod TCs failed before quenching start and there is nothing to compare with the results of calculation. In Fig. 25 and 26 the experimentally measured temperatures in the central rod pellet centre at the elevations 950 and 850 mm and calculated temperature evolutions at these elevations at the quenching phase of the test are presented. Finally, in Fig. 27

the experimentally measured temperatures of the shroud thermocouples TSH 11/0_I and TSH 11/180_I and the calculated temperatures of the rod outer surface at the elevation 750 mm at the quenching phase of the test are shown. In this last case the thermocouples located at the rod outer surface failed before quenching phase. The shroud TCs protected from direct contact with water-steam mixture show slow cool-down behaviour in the time period after 13459 sec. in contrast with the calculated temperature curve. Sharp drop of the calculated curve corresponds to the wetting of the rod surface.

Generally, calculated temperature evolution curves at the quenching phase of the test demonstrate rather good correlation with the experimental ones with respect to cool-down rate in the increasing steam flow and to the behaviour under rewetting conditions.

4.2 Oxide layer thickness

Similarly to the Q-07 and Q-08 tests simulation [6-8], in the presented work at first the main attention was paid to the comparison of the calculated oxide layer axial profile with the measured one. The experimental information about the oxide layer thickness is available at 11373 s when the corner rod **B** was withdrawn, at 13275 s when the corner rod **D** was withdrawn and at the end of the experiment.

Radial temperature distribution inside the bundle during the Q-10 test was generally close to uniform [9-10] which was the case for other quench bundle tests [4, 6, 8]. However, some difference in the averaged oxide thickness of the corner rods and of the heated rods (final status, see below, Fig. 30) points to some radial temperature difference. Nevertheless, comparison of the calculated central rod oxide thickness with that of corner rod during the test seems to be quite reasonable.

The obtained simulation results show that at the time moment 11373 s calculated oxide thickness is in good agreement with the experimental data (Fig. 28).

For the corner rod **D** withdrawn at 13275 s the experimental data on the oxide thickness are available only up to the elevation 850 mm because of the disintegration of the upper part of the rod. In Fig. 29 the comparison of the calculated oxide thickness with the available experimental data at the above mentioned time moment is presented. As one can see, the calculation results quite well correlate with the experimental data. However, one can expect some underestimation of the oxide thickness at the elevation 950 mm since there is certain difference of the calculated and experimental curves slope at 850 mm.

In Fig. 30 the averaged oxide layer thickness profiles of the heated rods and of the corner rods, measured at the end of the test are compared with the calculated oxide layer thickness profile of the central rod (final status). As one can see, the calculated oxide profile generally reproduces the measured ones. However, certain underestimation of the oxide thickness at the elevations 850 mm and 1000 mm takes place.

Since oxidation kinetics strongly depends on temperature, one may conclude that simulated temperature of some parts of the central rod was somewhat lower than the real temperature

of the heated rods during time period from 13275 s to the end of the test. This fact will lead to a certain underestimation of the hydrogen release rate described in the following subsection.

4.3 Hydrogen release analysis

Due to mentioned above uniformity of the radial temperature distribution inside the bundle one can say that the central rod behaviour generally represents the average behaviour of the 20 heated rods and shroud in a QUENCH bundle test. Using this consideration one can extrapolate the hydrogen production results calculated for the central rod to the whole bundle [4-8]. The total hydrogen production rate of the whole bundle $\dot{m}_{bundle}$ is connected with calculated central rod production rate $\dot{m}_{rod}$ by the following relation:

$$\dot{m}_{bundle} = \dot{m}_{rod}\left(N_{heated} + 1 + N_{corner}\frac{R_{corner}}{R_{rod}} + \frac{R_{shroud}}{R_{rod}} \right), \tag{19}$$

Here $N_{heated} = 20$ is the number of heated rods, $N_{corner} = 4$ is the number of corner rods, R_{corner}, R_{rod} and R_{shroud} are heated rod, corner rod and shroud radii correspondingly.

In Fig. 31 hydrogen production rate calculated according to relation (20) on the basis of S/Q code simulation and the experimental data are presented. As one can see, the calculated curve repeats all the bents and curvatures of the experimental one during the preoxidation phase of the test, but is located lower.

The variations of the hydrogen production during preoxidation are determined by the competition of the two factors: (i) increasing temperature, which leads to intensification of oxidation and thus, to increase of the hydrogen production rate and (ii) growing oxide thickness leading to decrease of the oxidation and hydrogen production rates. Moreover, in the conditions of QUENCH bundle experiments temperature and oxide thickness are *axially distributed* values (different elevations contribute to hydrogen production differently).

These considerations explain complicated behaviour of the hydrogen production rate at the preoxidation phase of the test when temperature varied rather smoothly or was even close to constant. Reproduction of the experimental curve's shape by the S/Q code indicates that Zr oxidation kinetics is quite correctly described by the code.

As for the underestimation of the absolute value of the hydrogen production rate during preoxidation phase of the test, one should consider the following. Oxidation model of the S/Q code is based on the mass conservation relations: every oxygen atom penetrating Zr/steam boundary corresponds to one released hydrogen molecule. Thus, there exists direct correspondence between oxide layer thickness axial profile and amount of produced hydrogen, accurately accounted by the code.

During the whole preoxidation phase the calculated hydrogen production rate was noticeably lower then the experimental one. At the same time, calculated oxide axial profile at the end of the preoxidation phase of the test (time moment 11373 s, see previous subsection, Fig. 28) quite well agrees with the experimental profile. Here one has a 'mass balance' contradiction

and the reason of this contradiction is not clear. The revealed discrepancy can be only *partially* explained by the fact that not all the oxidizing materials presented in the bundle were taken into account in the calculations (e.g. spacer grids, thermocouples shields).

In Fig. 31 the calculated and measured hydrogen production rate at the quenching phase of the test are presented. As one can see, the experimental production peak takes place several seconds later (due to the location of mass spectrometer) and is much higher than the calculated one. This fact may be explained by some underestimation of the temperature peaks by the S/Q code during temperature escalation in the upper part of the bundle (Fig. 22-24) as well as by possible measurement errors.

According to the calculation results, the total amount of generated hydrogen is 34.8 g (3.4 g during quenching). As it is clear from the above considerations, these values are lower than the experimental ones (54.5 g and 5.2 g, correspondingly [9]).

5 Summary and conclusions

- SVECHA/QUENCH code was applied to the simulation of the QUENCH bundle test Q-10. The simulation was performed within the framework of the 'effective channel approach'.

- The experimentally measured temperatures of the heated rods were processed, smoothed and then used as boundary conditions (average temperature field) for the central rod.

- The simulation of the Q-10 test using averaged temperature field was performed. All the stages of the test (heatup, preoxidation, transient, air ingression, water quenching) were considered.

- Since the specific model of zirconium-nitrogen physical-chemical interaction has not been yet developed and implemented in the S/Q code, only oxygen interaction with Zr cladding as the main air component was described.

- The calculations adequately reproduce temperature evolution of the central rod at different elevations during the whole test duration including quenching phase.

- The calculated oxide axial profile agrees quite well with the experimental data at the time moments 11373 s and 13275 s when the corner rods B and D were withdrawn from the bundle. The S/Q code slightly underestimates final oxide thickness.

- The details of the experimentally measured time dependence of the hydrogen production rate during preoxidation phase of the test are well reproduced by the calculations. This fact testifies that Zr oxidation kinetics is quite correctly described by the S/Q code. At the same time, absolute value of the hydrogen production rate appears to be underestimated, in 'mass balance' contradiction with oxide axial profile correct reproduction by the calculations.

Acknowledgements

The author is grateful to Dr. J. Stuckert for his interest to this work, important comments and fruitful discussions.

References

1. *P.Hofmann, V.Noack, M.S.Veshchunov, A.V.Berdyshev, A.V.Boldyrev, L.V.Matweev, A.V.Palagin, V.E.Shestak,* Physico-Chemical Behavior of Zircaloy Fuel Rod Cladding Tubes During LWR Severe Accident Reflood, FZKA 5846, 1997;

2. *P.Hofmann, A.Miassoedov, L.Steinbock, M.Steinbrueck, M.S.Veshchunov, A.V.Berdyshev, A.V.Boldyrev, A.V.Palagin, V.E.Shestak*, Quench Bechaviour of Zircaloy Fuel Rod Cladding Tubes. Small-Scale Experiments and Modeling of the Quench Phenomena, FZKA 6208, 1998;

3. *A.V.Berdyshev, A.V.Boldyrev, A.V.Palagin, V.E.Shestak, M.S.Veshchunov*, SVECHA/QUENCH Code for The Modeling of Reflooding Phenomena in Severe Accidents Conditions. Proceedings of the Ninth International Topical Meeting on Nuclear Reactor Thermal Hydraulics (NURETH-9), paper Log_19 (CD-ROM edition), San Francisco, California, USA, October 1999;

4. *L.Sepold, P.Hofmann, C.Homann, W.Leiling, A.Miassoedov, D.Piel, G.Schanz, L.Schmidt, U.Stegmaier, M.Steinbrueck, H.Steiner, A.V.Palagin, A.V.Boldyrev, M.S.Veshchunov, A.V.Berdyshev, V.E.Shestak*, Investigation of an Overheated PWR-Type Fuel Rod Simulator Bundle, FZKA 6412, 2001;

5. *M.S.Veshchunov, A.V.Boldyrev, A.V.Palagin, V.E.Shestak*. Application of the SVE-CHA/QUENCH code to the simulation of the QUENCH bundle test Q-07. IBRAE Report NSI-SARR-184-04, Moscow, December 2004;

6. *M.S.Veshchunov, A.V.Berdyshev, A.V.Boldyrev, A.V.Palagin, V.E.Shestak, M.Steinbrück, J.Stuckert*. Modelling of B_4C oxidation by steam at high temperatures based on separate-effects tests and its application to the bundle experiment QUENCH-07, FZKA 7118, 2005;

7. *M.S.Veshchunov, A.V.Boldyrev, A.V.Palagin, V.E.Shestak*. Application of the SVE-CHA/QUENCH code to the simulation of the QUENCH bundle test Q-08. IBRAE Report NSI-SARR-189-05, Moscow, June 2005;

8. *J.Stuckert, A.V.Boldyrev, A.Miassoedov, A.V.Palagin, G.Schanz, L.Sepold, V.E.Shestak, U.Stegmaier, L.Steinbock, M.Steinbrück, H.Steiner, M.S.Veshchunov*, Experimental and Computational Results of the QUENCH-08 Experiment (Reference to QUENCH-07) FZKA 6970, 2005;

9. *L.Sepold, L.Steinbock, M.Steinbrück, U.Stegmaier, J.Stuckert, A.Miassoedov, S.Horn, Z.Hozer, I.Nagy, P.Windberg, L.Matus.* Interner Bericht, Forschungszentrum Karlsruhe, October 2004;

10. *G.Schanz, M.Heck, Z.Hozer, L.Matus, I.Nagy, L.Sepold, U.Stegmaier, M.Steinbrück, H.Steiner, J.Stuckert, P.Windberg.* Results of the QUENCH-10 Experiment on Air Ingress, FZKA 7087, 2006;

11. *M.S.Veshchunov, A.V.Berdyshev, A.V.Boldyrev, A.V.Palagin, V.E.Shestak*. Modelling of LWR Core Quench Phenomena. Part IV. IBRAE Report, Moscow, December 1999;

12. SCDAP/RELAP5/MOD2 Code Manual, Volume 4: MATPRO – A Library of Materials Properties for Light-Water-Reactor Accident Analysis. NUREG/CR-5273 EGG-2555. Vol.4. 1990;

13. Handbook of Physical Quantities, *I.S.Grigoriev, E.Z.Meilikhov*, Eds., CRC Press, 1997;

14. *R.S.Brokaw*, Predicting Transport Properties of Dilute Gases, IREC Process Design and Development, 8, 1969, pp. 240-253;

15. *R.B.Bird, W.E.Stewart, E.N.Lightfoot,* Transport Phenomena, New York: John Wiley and Sons, Inc., 1954;

16. *D.R.Olander*, Nucl. Eng. Des. 148 (1994) 253-271.

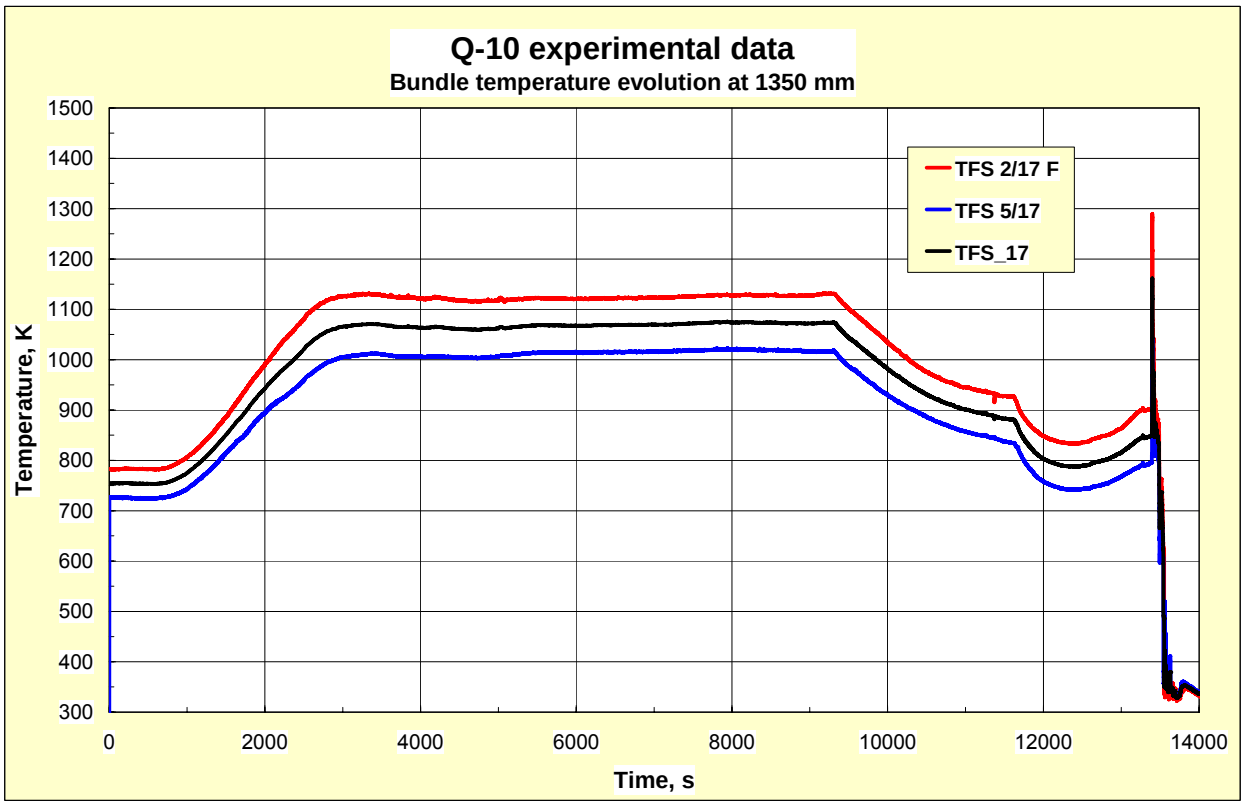

Fig 1. Bundle temperature evolution at the elevation 1350 mm measured by thermocouples TFS 2/17 (red line), TFS 5/17 (blue line) and averaged temperature used in the calculations (black line).

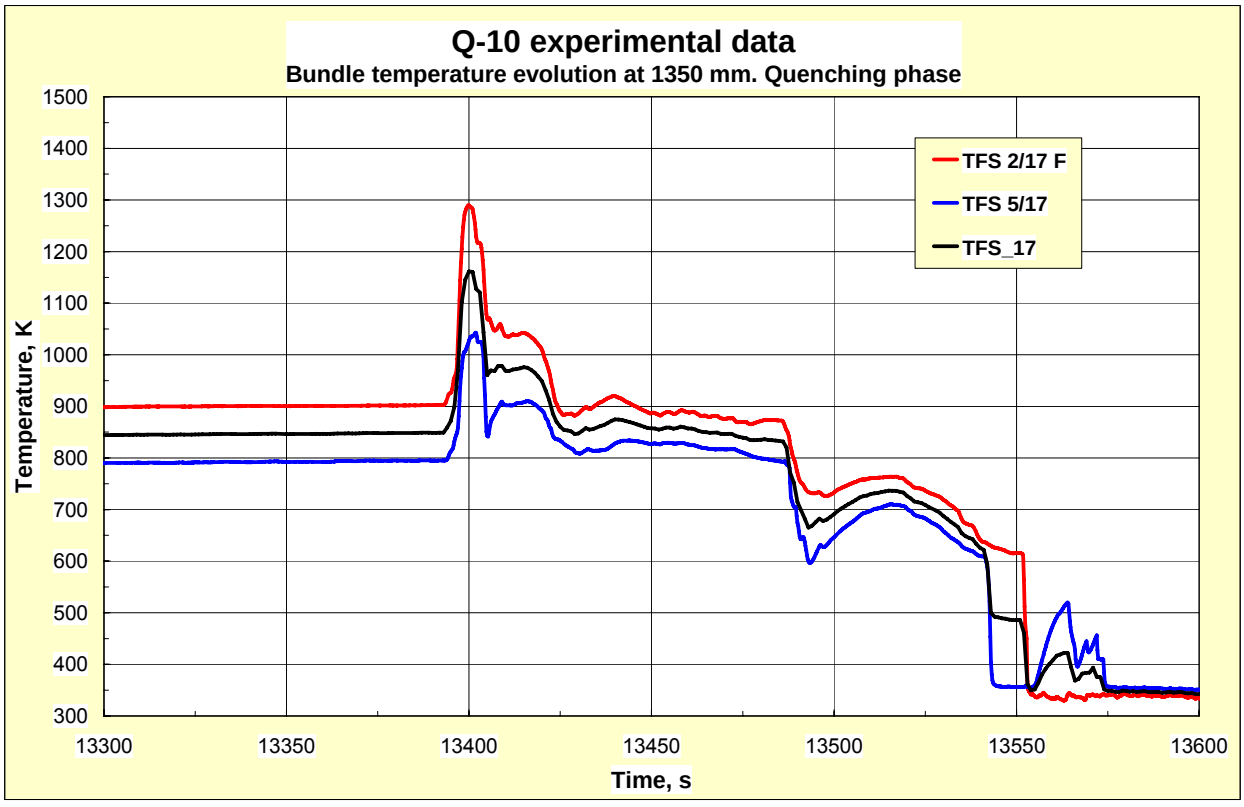

Fig 2. Bundle temperature evolution at the elevation 1350 mm measured by thermocouples TFS 2/17 (red line), TFS 5/17 (blue line) and averaged temperature used in the calculations (black line). Quenching phase (time period 13300 – 13600 s).

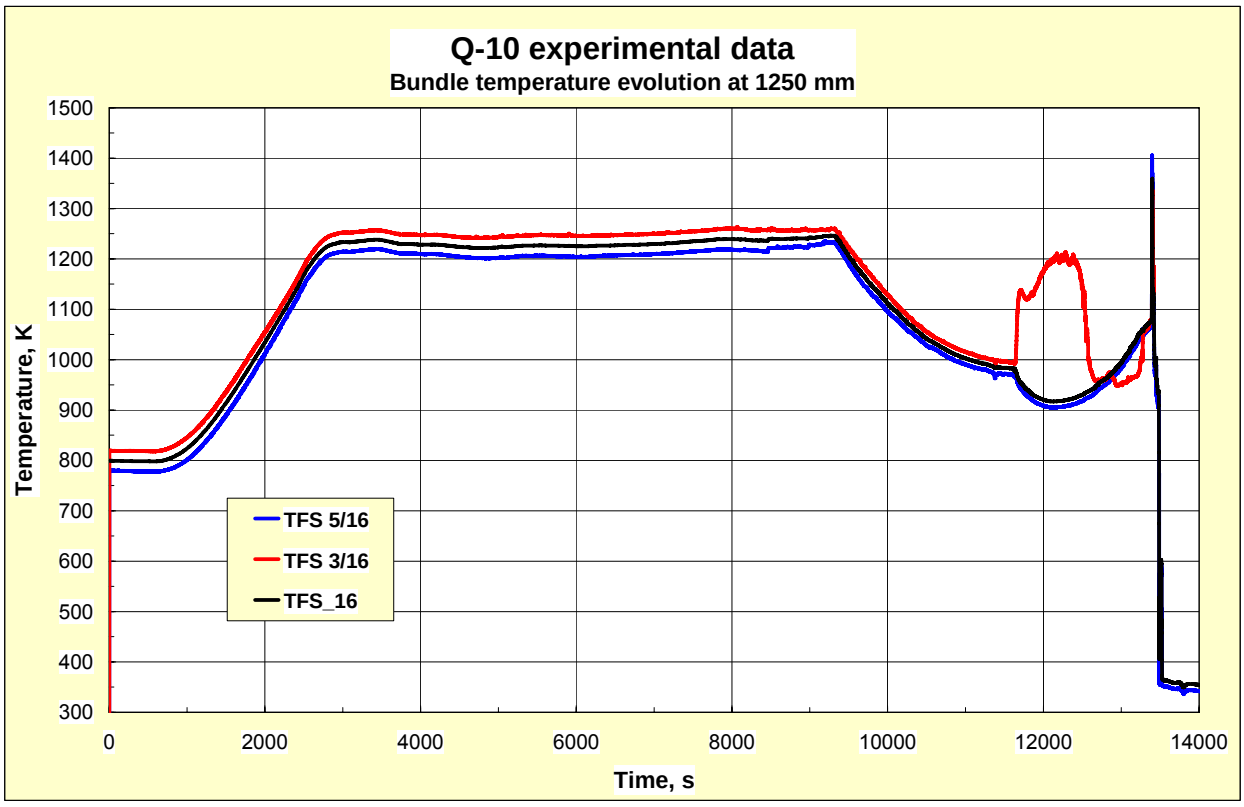

Fig 3. Bundle temperature evolution at the elevation 1250 mm measured by thermocouples TFS 3/16 (red line), TFS 5/16 (blue line) and averaged temperature used in the calculations (black line).

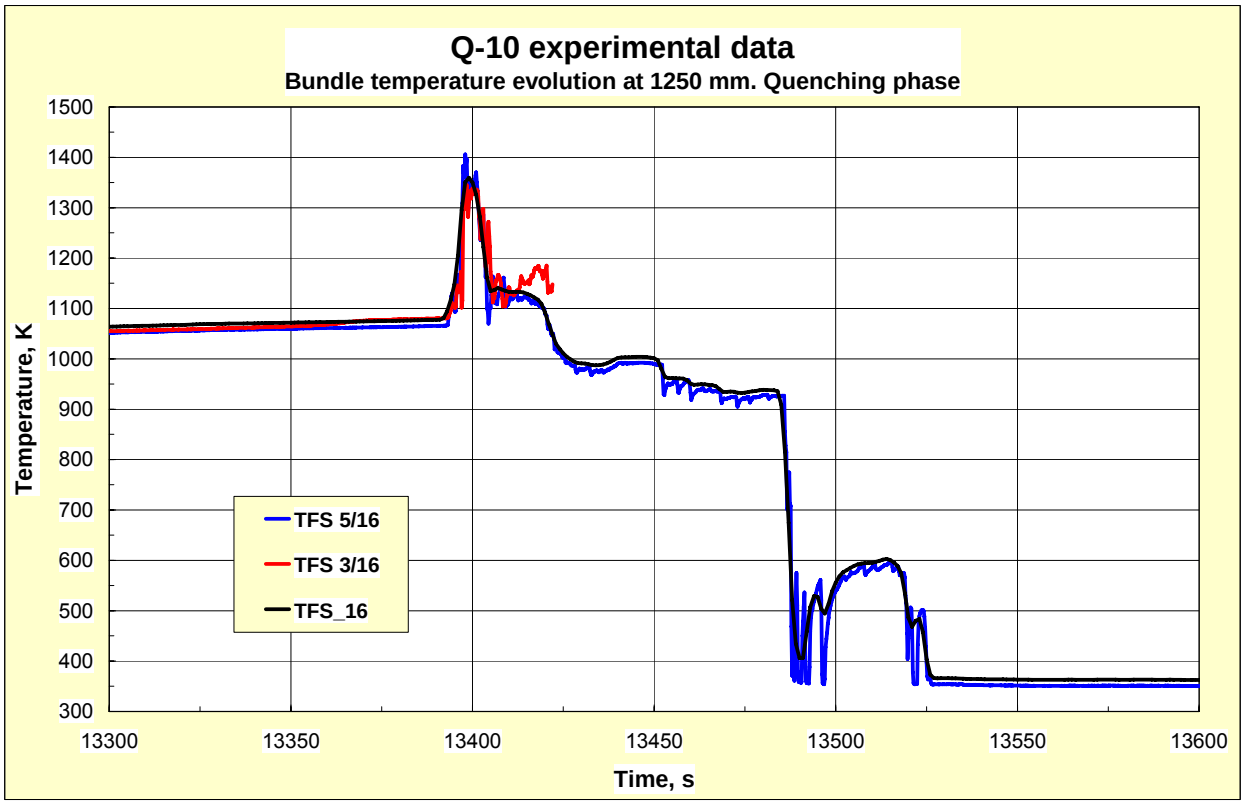

Fig 4. Bundle temperature evolution at the elevation 1250 mm measured by thermocouples TFS 3/16 (red line), TFS 5/16 (blue line) and averaged temperature used in the calculations (black line). Quenching phase (time period 13300 – 13600 s).

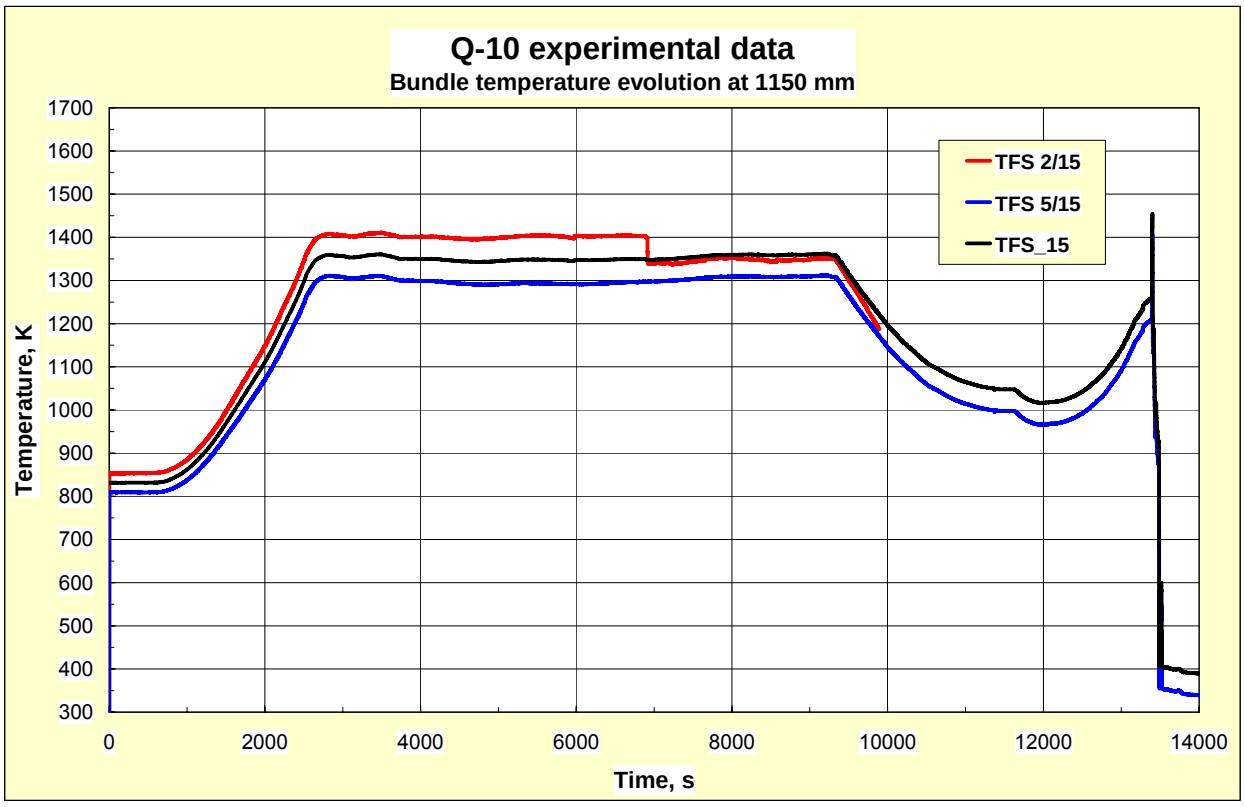

Fig 5. Bundle temperature evolution at the elevation 1150 mm measured by thermocouples TFS 2/15 (red line), TFS 5/15 (blue line) and averaged temperature used in the calculations (black line).

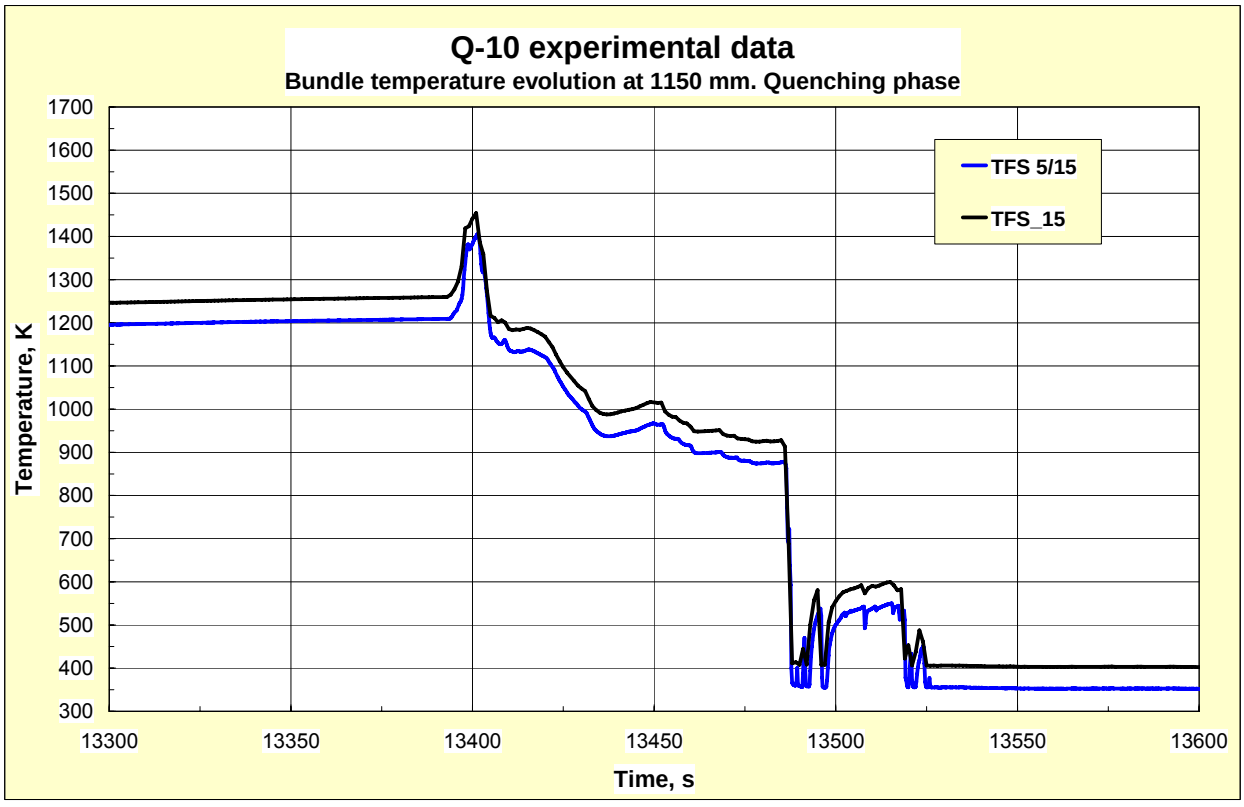

Fig 6. Bundle temperature evolution at the elevation 1150 mm measured by thermocouple TFS 5/15 (blue line) and averaged temperature used in the calculations (black line). Quenching phase (time period 13300 – 13600 s).

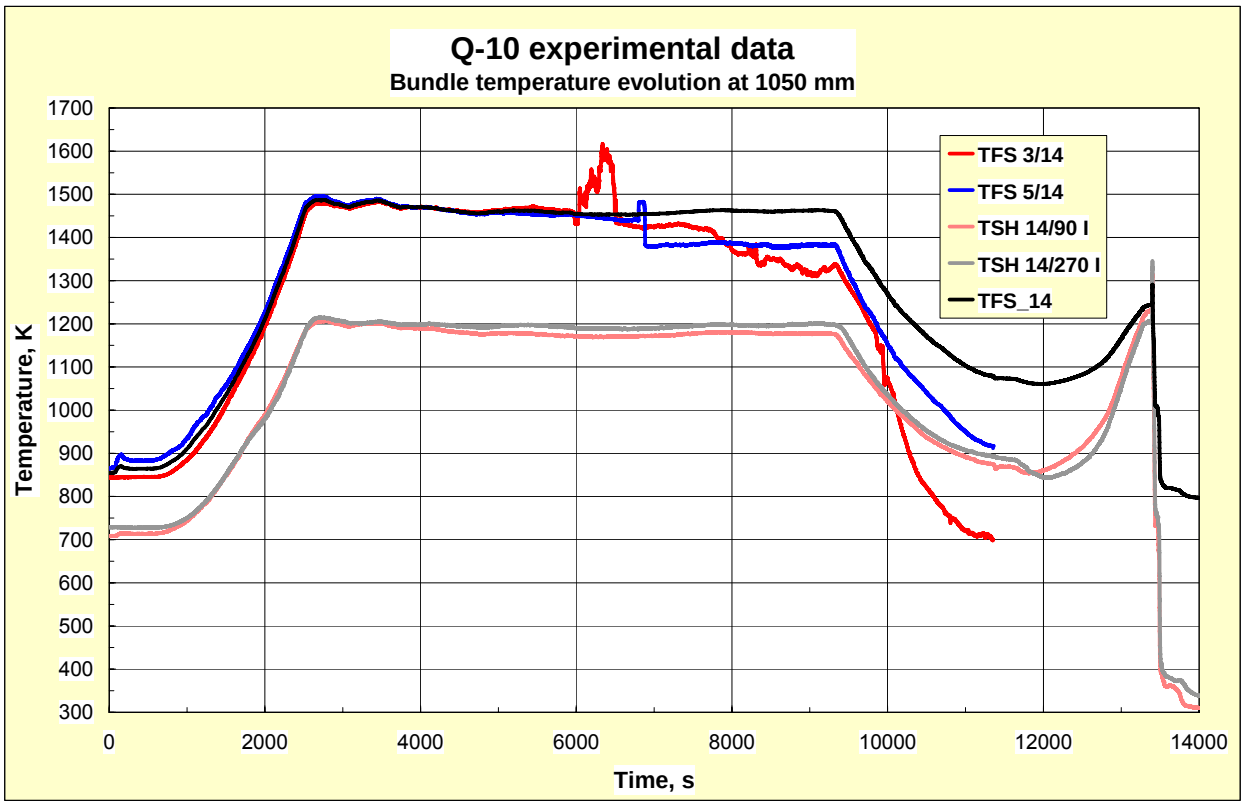

Fig 7. Bundle temperature evolution at the elevation 1050 mm measured by thermocouples TFS 3/14 (red line), TFS 5/14 (blue line), shroud thermocouples TSH 14/90_I (coral line), TSH 14/270_I (grey line) and averaged temperature used in the calculations (black line).

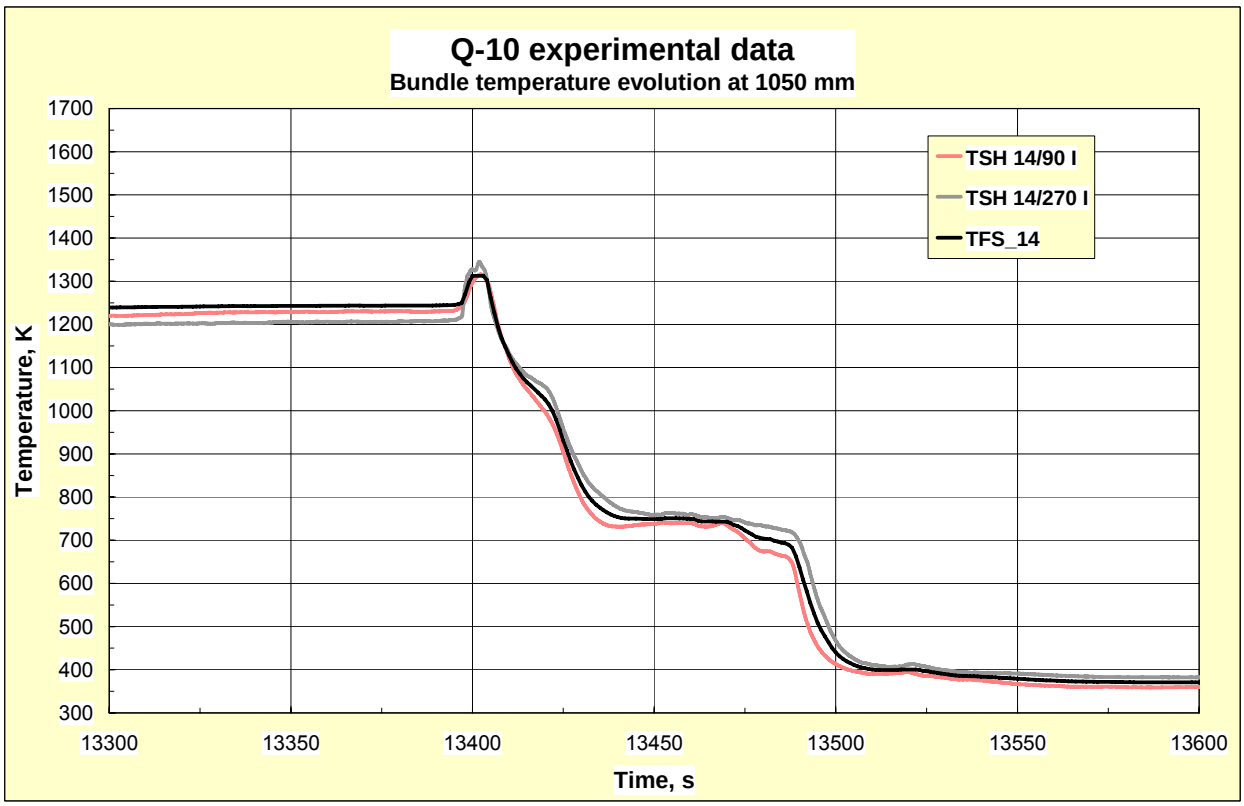

Fig 8. Bundle temperature evolution at the elevation 1050 mm measured by shroud thermocouples TSH 14/90_I (coral line), TSH 14/270_I (grey line) and averaged temperature used in the calculations (black line). Quenching phase (time period 13300 – 13600 s).

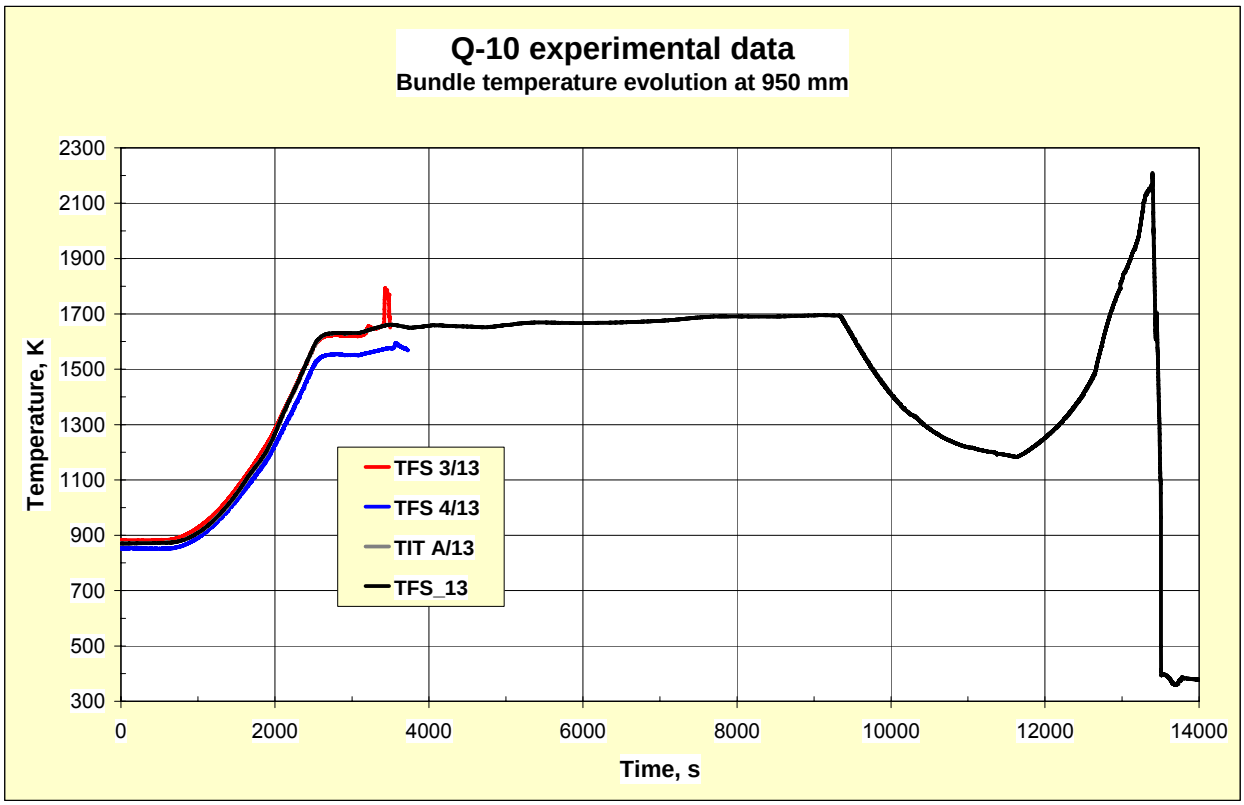

Fig 9. Bundle temperature evolution at the elevation 950 mm measured by thermocouples TFS 3/13 (red line), TFS 4/13 (blue line), corner rod thermocouple TIT A/13 (grey line) and averaged temperature used in the calculations (black line, practically coincides with TIT A/13 data).

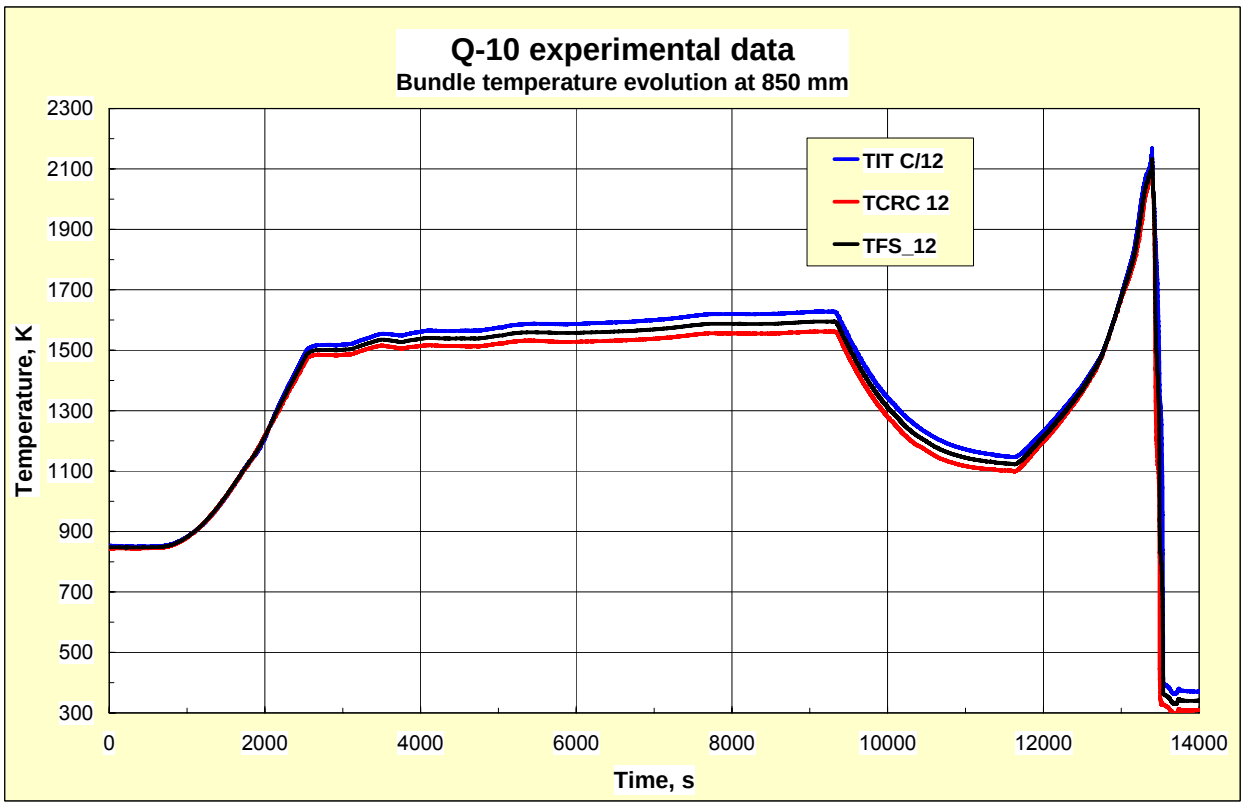

Fig 10. Bundle temperature evolution at the elevation 850 mm measured by corner rod thermocouple TIT C/12 (blue line), central rod internal thermocouple TCRC 12 (red line) and averaged temperature used in the calculations (black line).

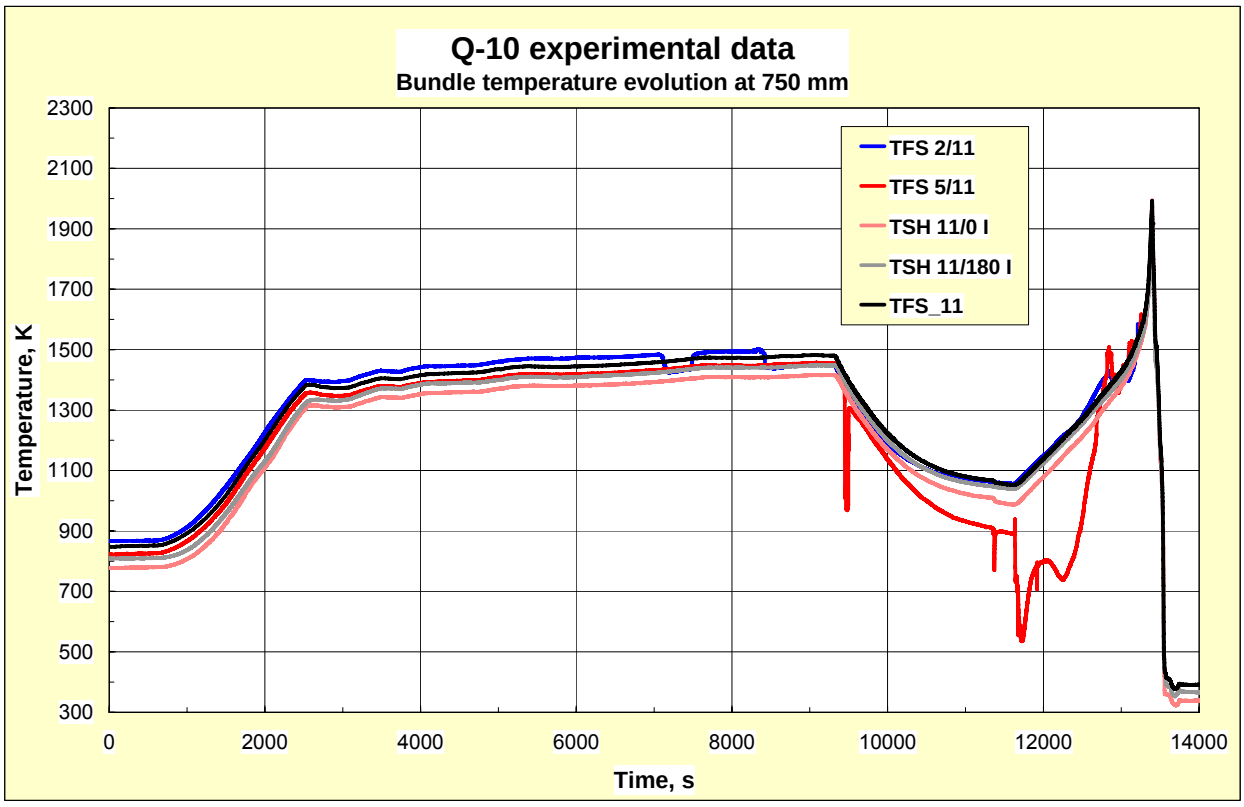

Fig 11. Bundle temperature evolution at the elevation 750 mm measured by thermocouples TFS 2/11 (blue line), TFS 5/11 (red line), shroud thermocouples TSH 11/0_I (coral line), TSH 11/180_I (grey line) and averaged temperature used in the calculations (black line).

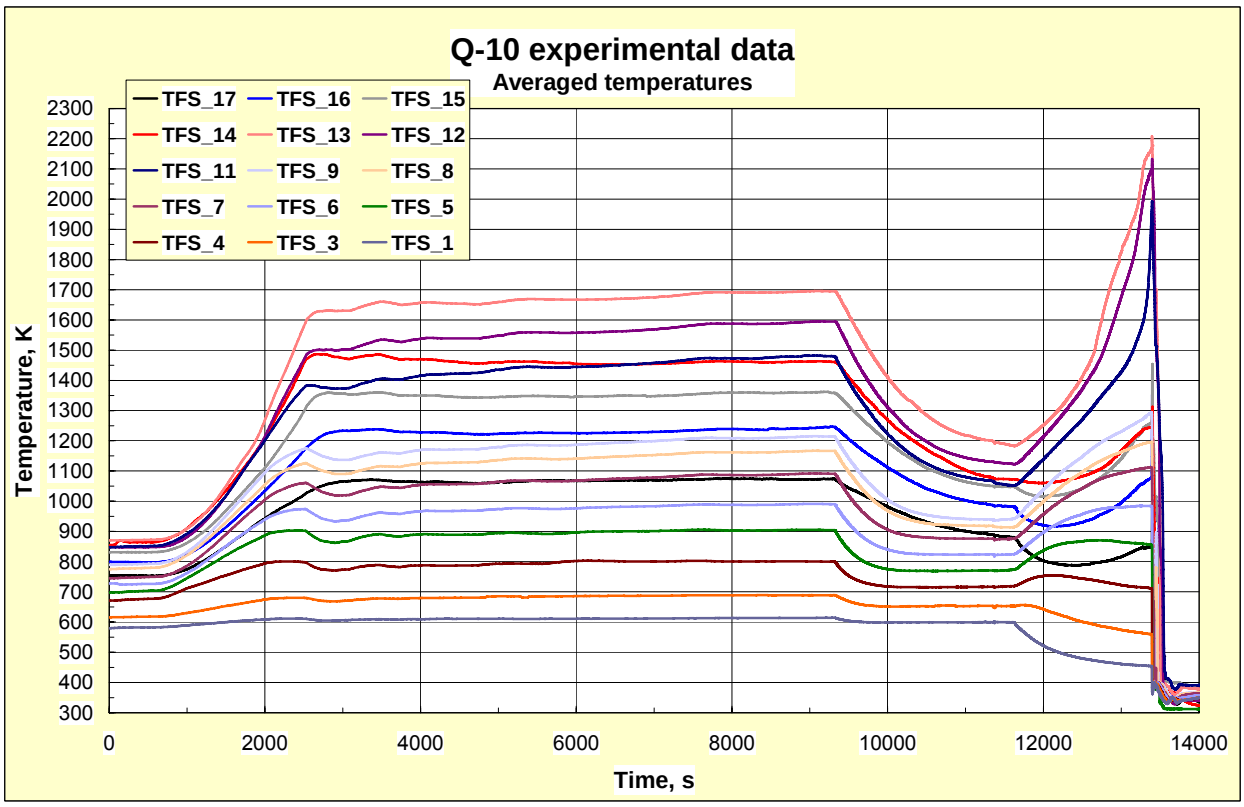

Fig 12. Averaged and smoothed curves representing temperature evolution of the QUENCH-10 bundle at the elevations from 1350 to -250 mm.

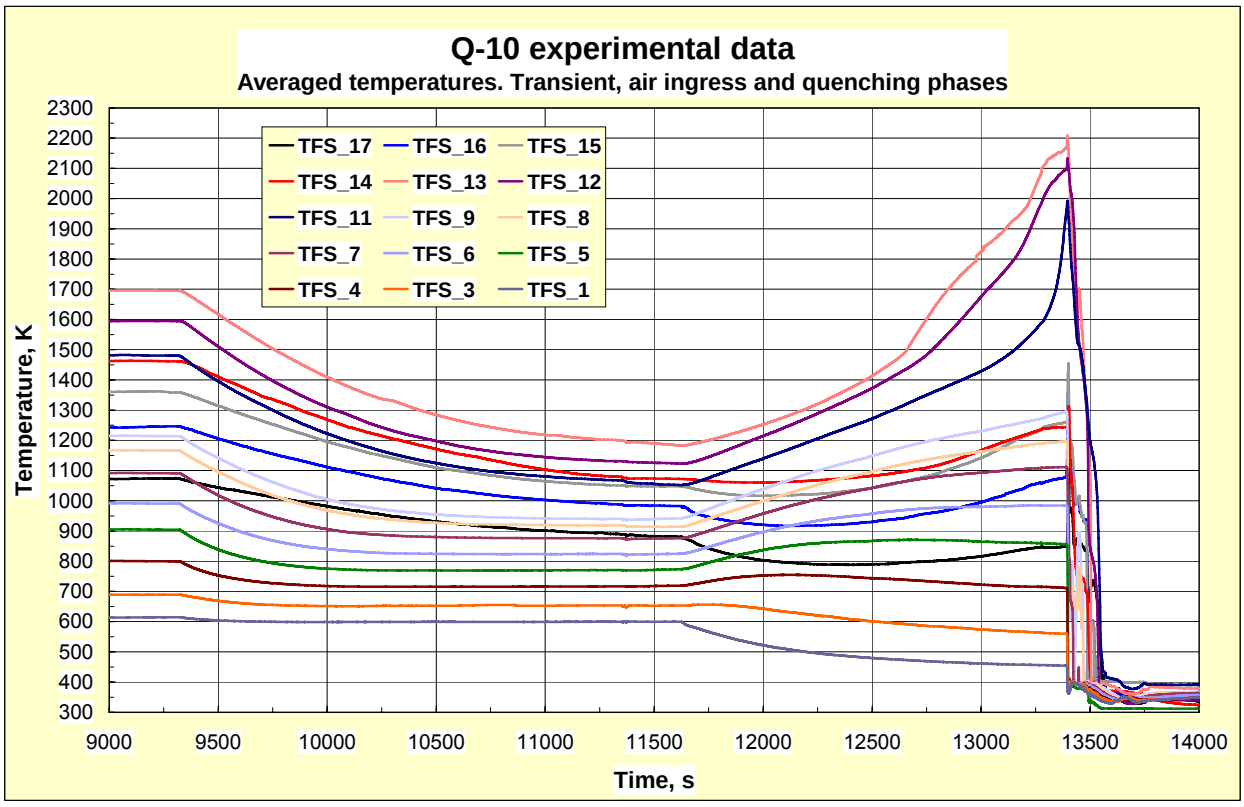

Fig 13. Averaged and smoothed curves representing temperature evolution of the QUENCH-10 bundle at the elevations from 1350 to -250 mm. Transient, air ingress and quenching phases of the test.

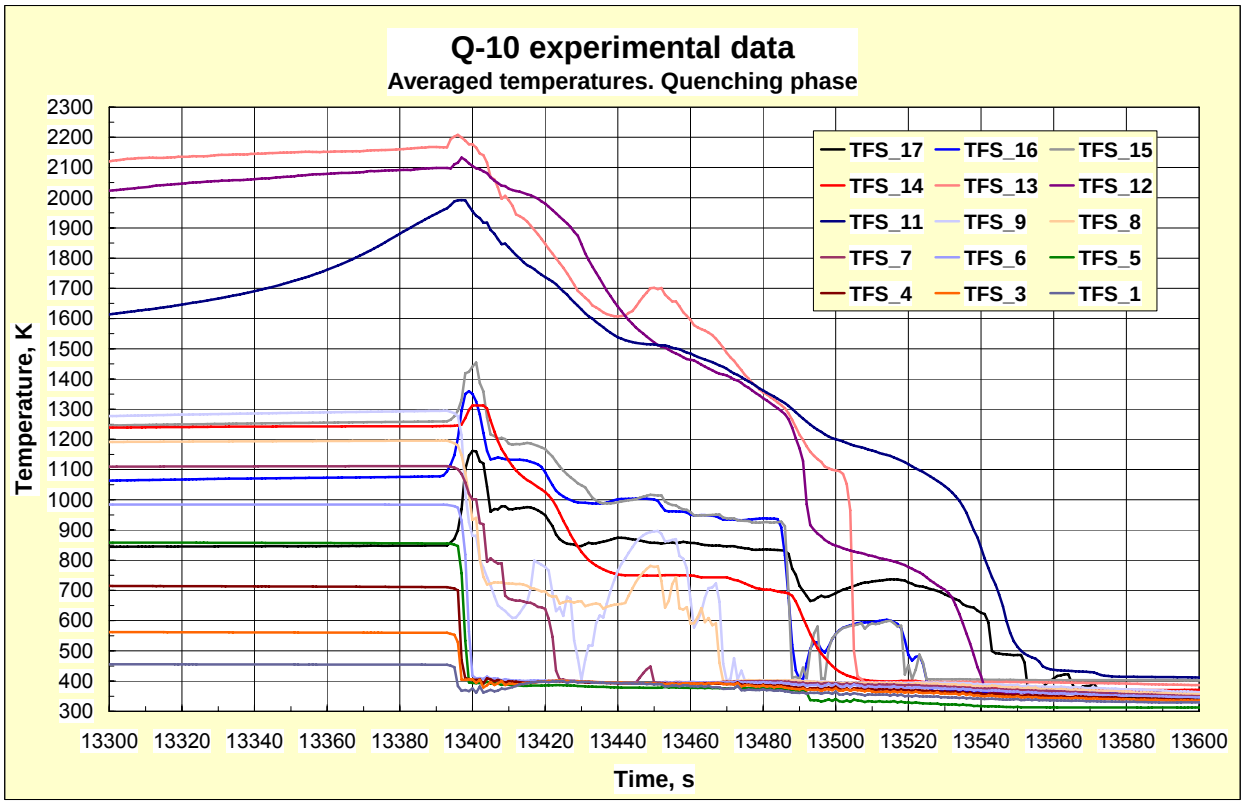

Fig 14. Averaged and smoothed curves representing temperature evolution of the QUENCH-10 bundle at the elevations from 1350 to -250 mm. Quenching phase of the test.

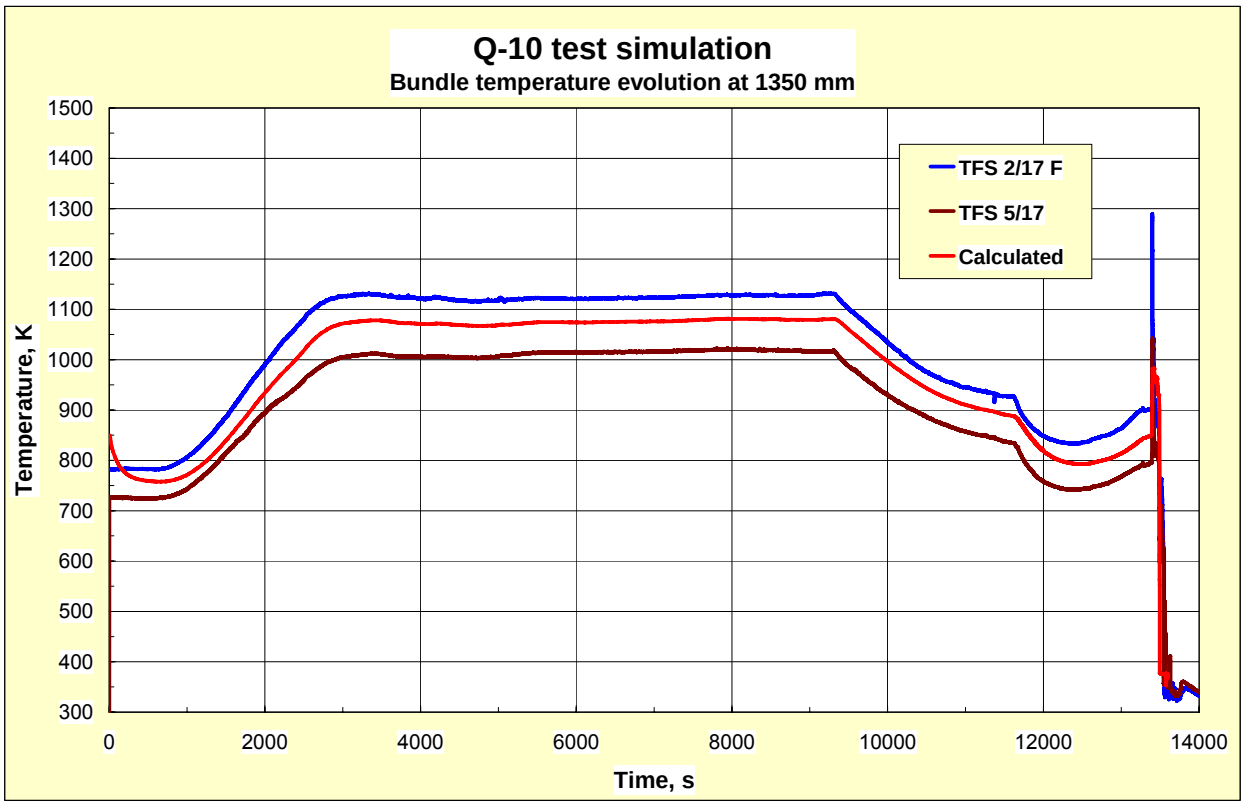

Fig 15. The experimentally measured temperatures at the elevation 1350 mm: TFS2/17 data (blue line) and TFS5/17 data (black line) and calculated temperature evolution of the central rod outer surface (red line).

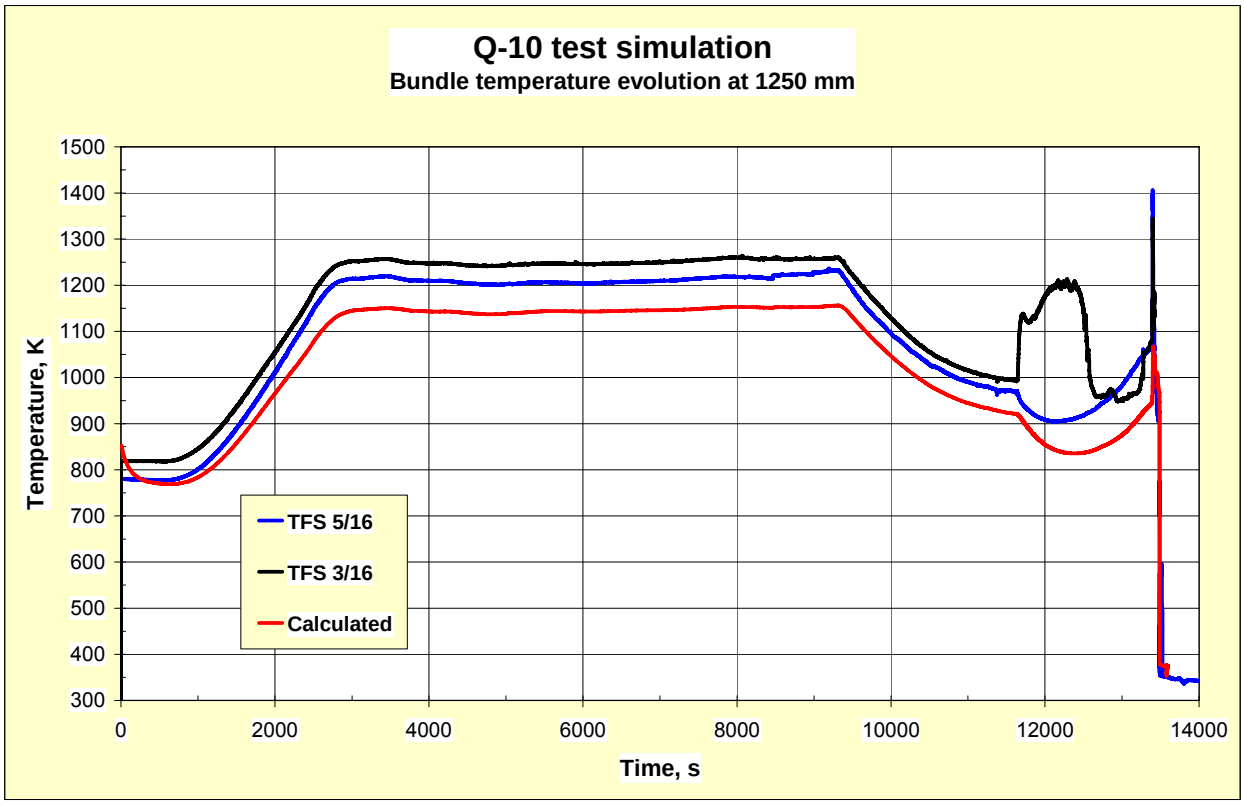

Fig 16. The experimentally measured temperatures at the elevation 1250 mm: TFS5/16 data (blue line) and TFS3/16 data (black line) and calculated temperature evolution of the central rod outer surface (red line).

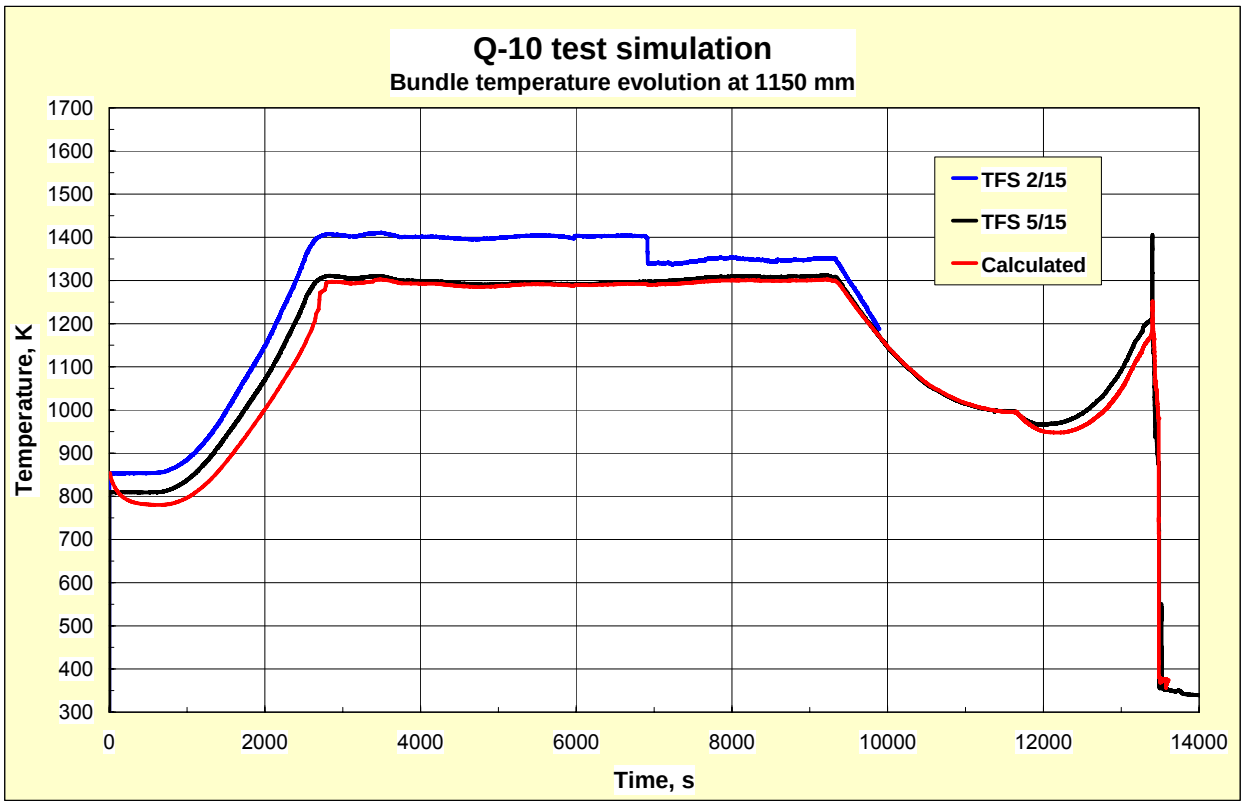

Fig 17. The experimentally measured temperatures at the elevation 1150 mm: TFS2/15 data (blue line) and TFS5/15 data (black line) and calculated temperature evolution of the central rod outer surface (red line).

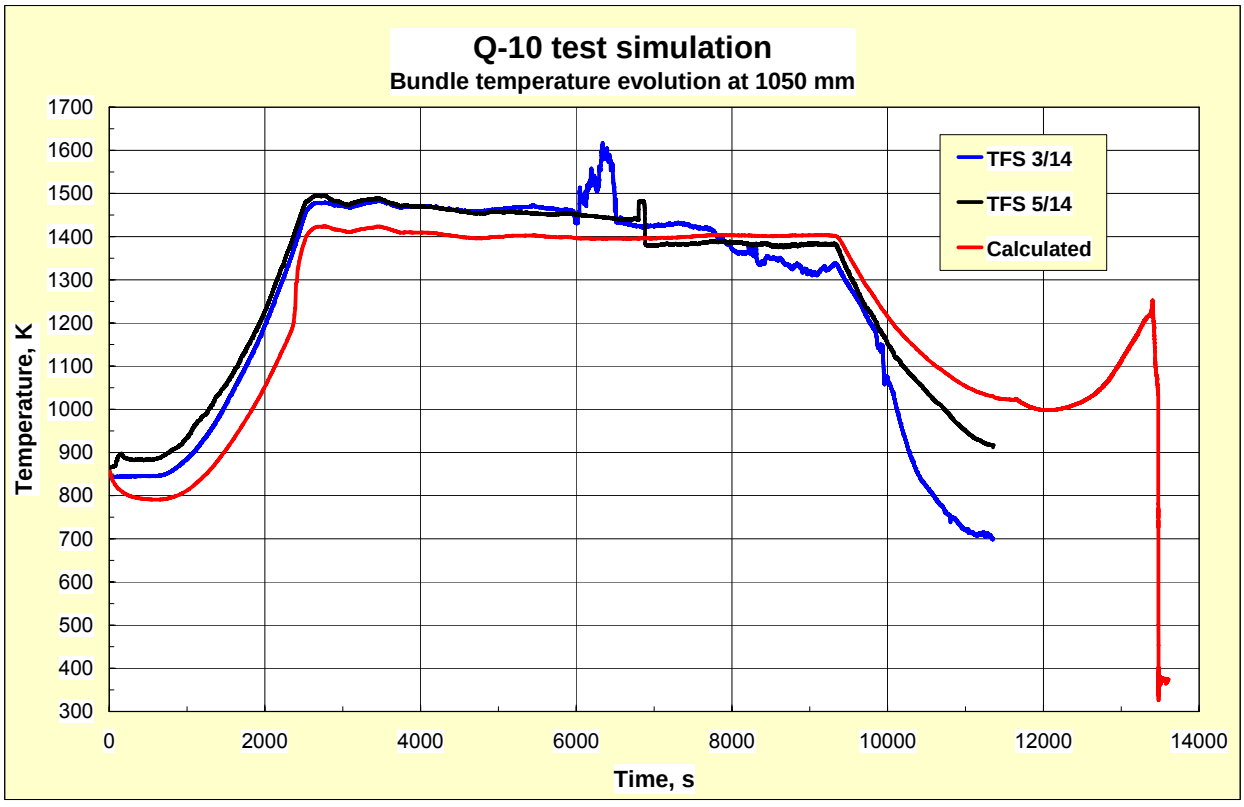

Fig 18. The experimentally measured temperatures at the elevation 1050 mm: TFS3/14 data (blue line) and TFS5/14 data (black line) and calculated temperature evolution of the central rod outer surface (red line).

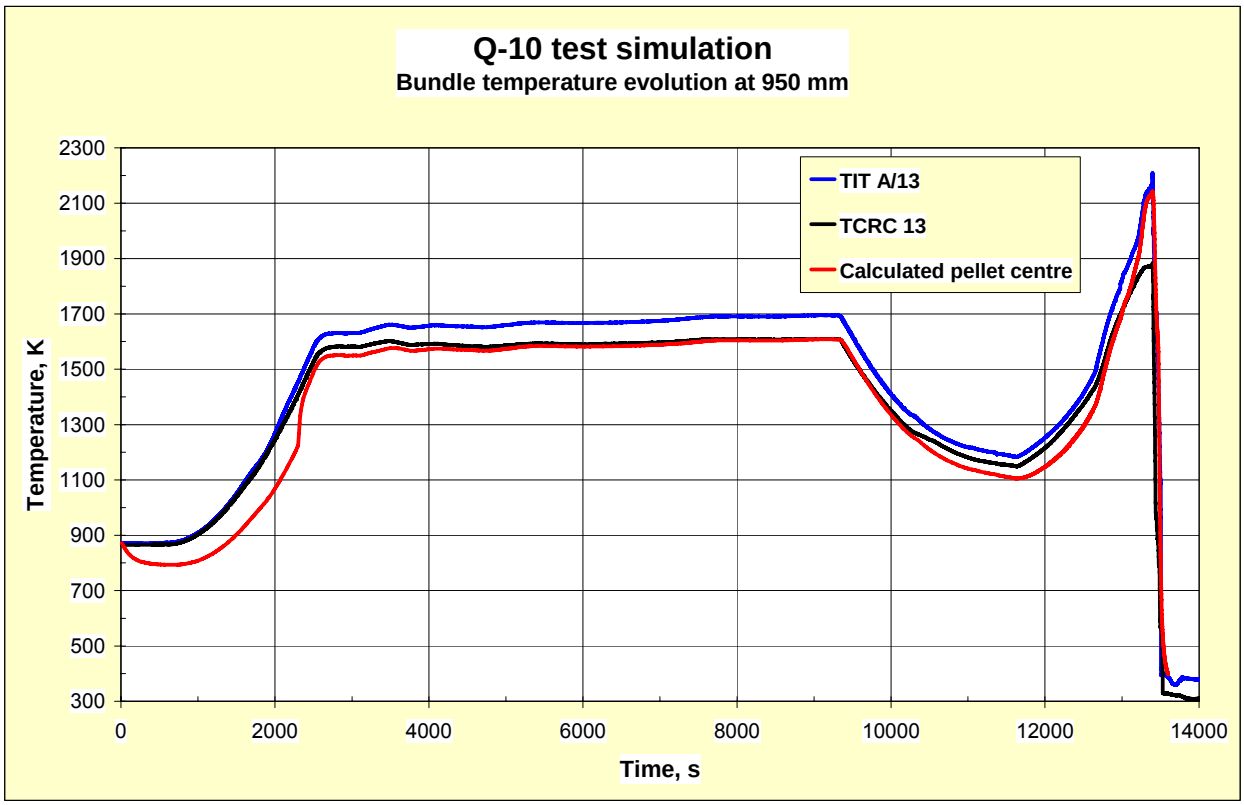

Fig 19. The experimentally measured temperatures at the elevation 950 mm: TIT A/13 data (blue line) and TCRC 13 data (black line) and calculated temperature evolution in the central rod pellet centre (red line).

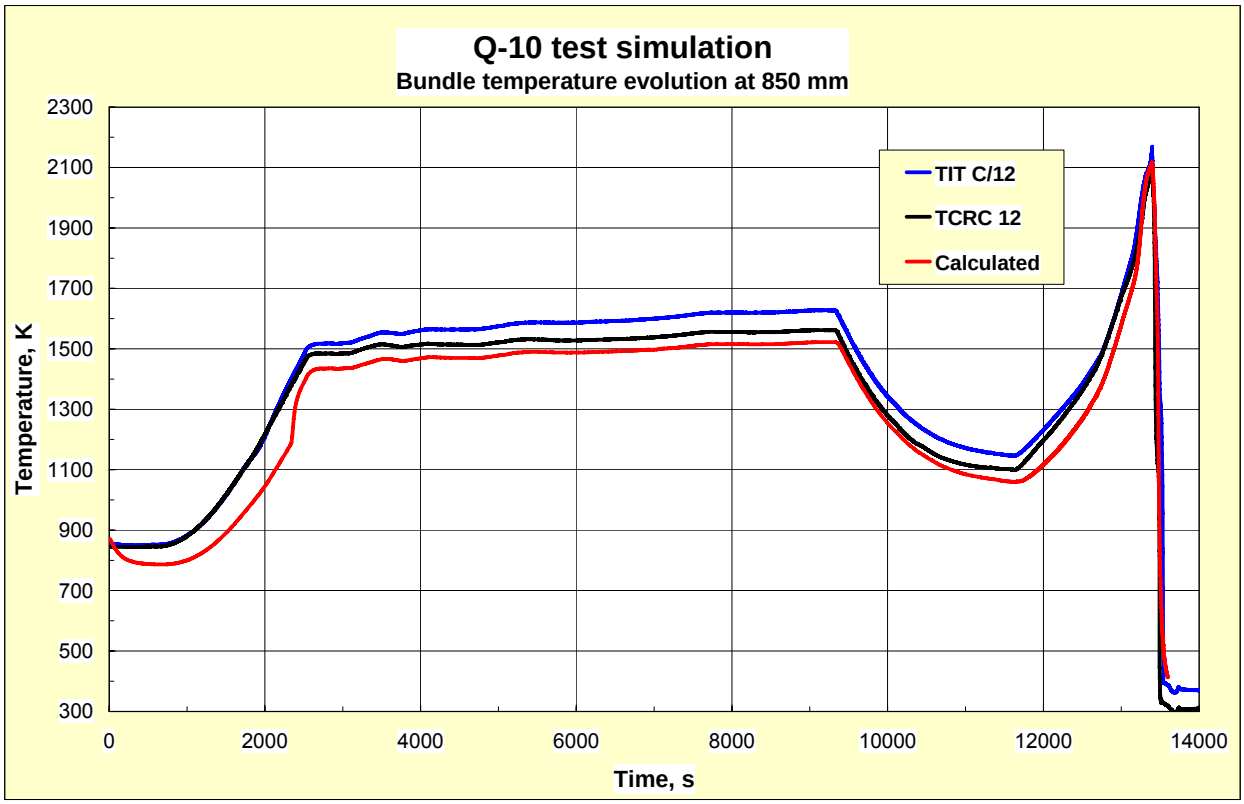

Fig 20. The experimentally measured temperatures at the elevation 850 mm: TIT C/12 data (blue line) and TCRC 12 data (black line) and calculated temperature evolution in the central rod pellet centre (red line).

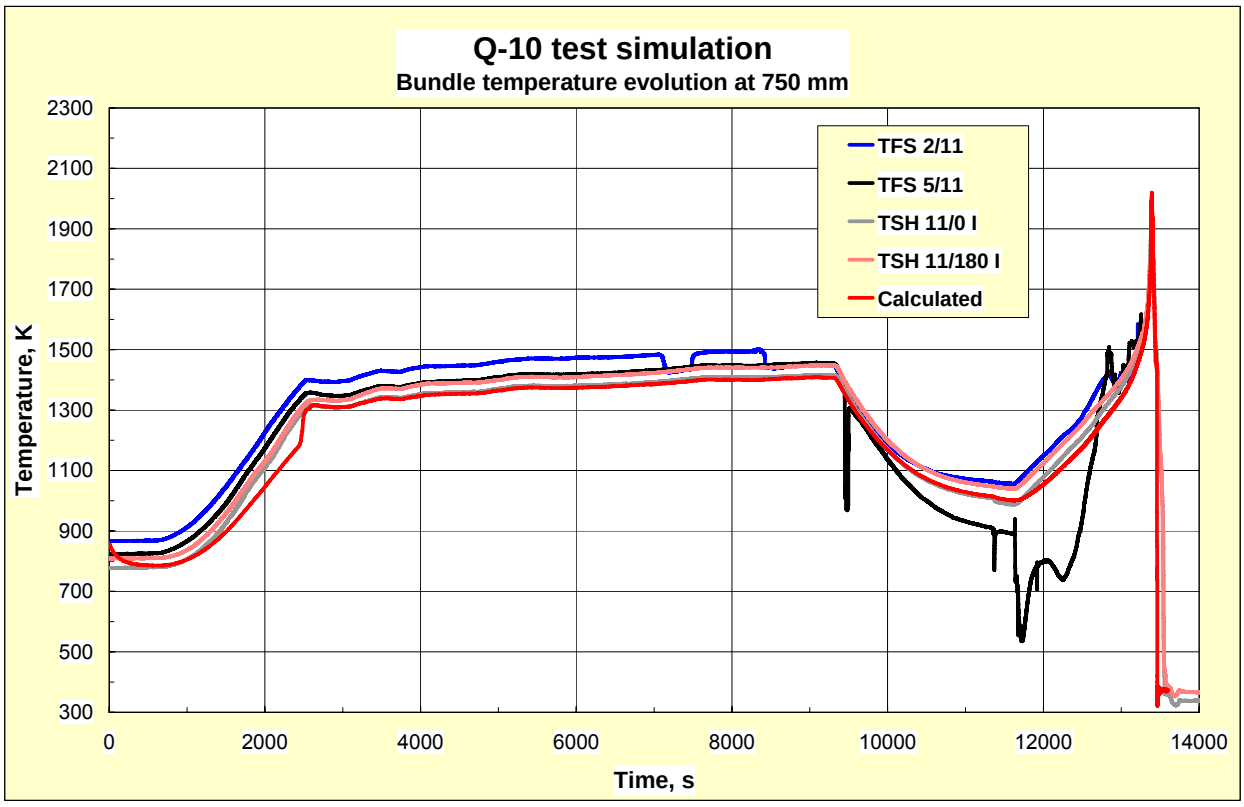

Fig 21. The experimentally measured temperatures at the elevation 750 mm: TFS 2/11 data (blue line), TFS 5/11 data (black line), TSH 11/0_I (grey line), TSH 11/180_I (coral line) and calculated temperature evolution of the central rod outer surface (red line).

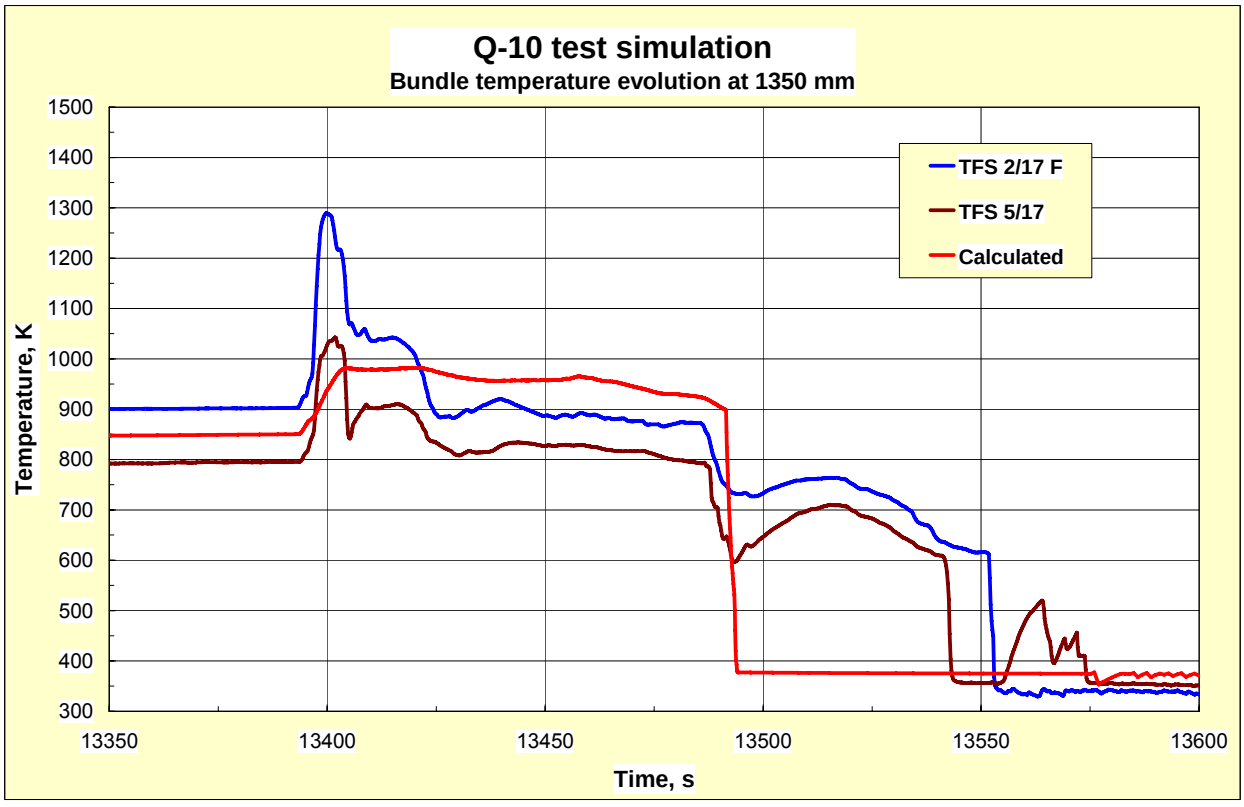

Fig 22. The experimentally measured temperatures at the elevation 1350 mm: TFS2/17 data (blue line) and TFS5/17 data (black line) and calculated temperature evolution of the central rod outer surface (red line). Quenching phase (time period 13350 – 13600 sec.).

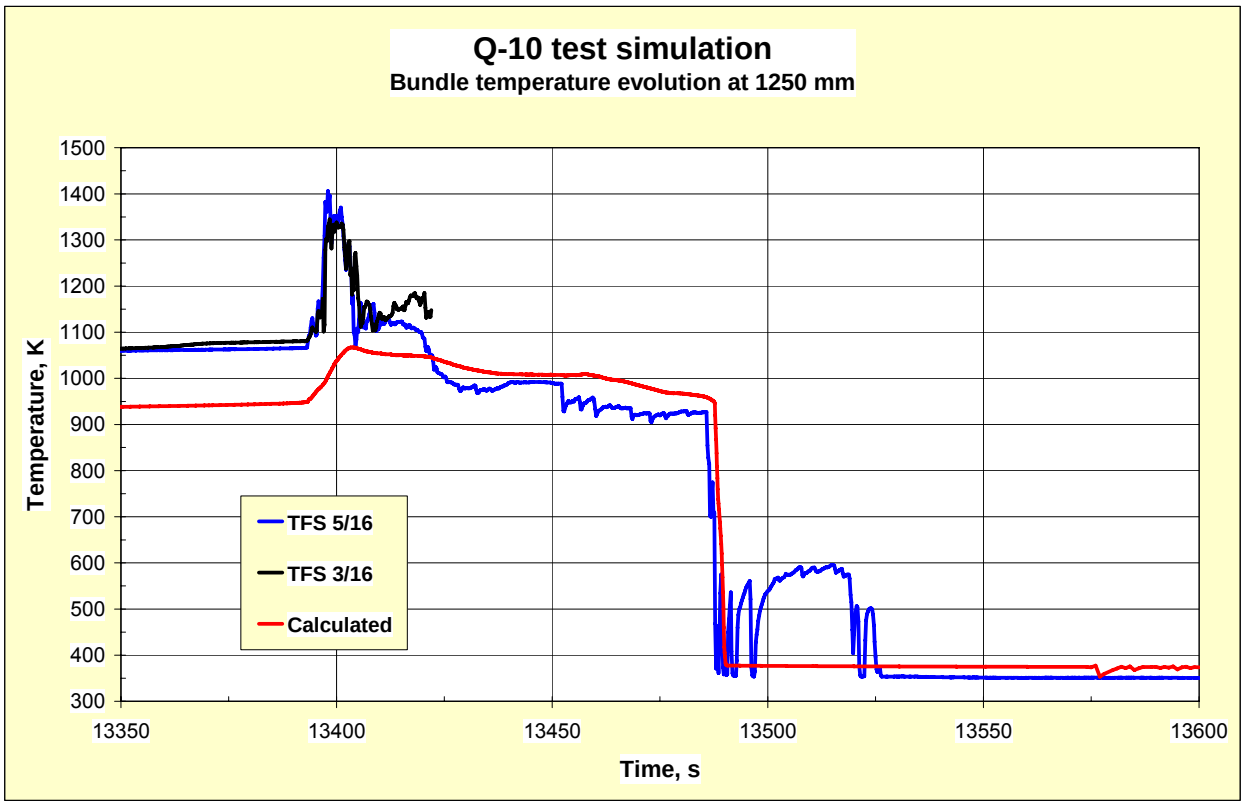

Fig 23. The experimentally measured temperatures at the elevation 1250 mm: TFS5/16 data (blue line) and TFS3/16 data (black line) and calculated temperature evolution of the central rod outer surface (red line). Quenching phase (time period 13350 – 13600 sec.).

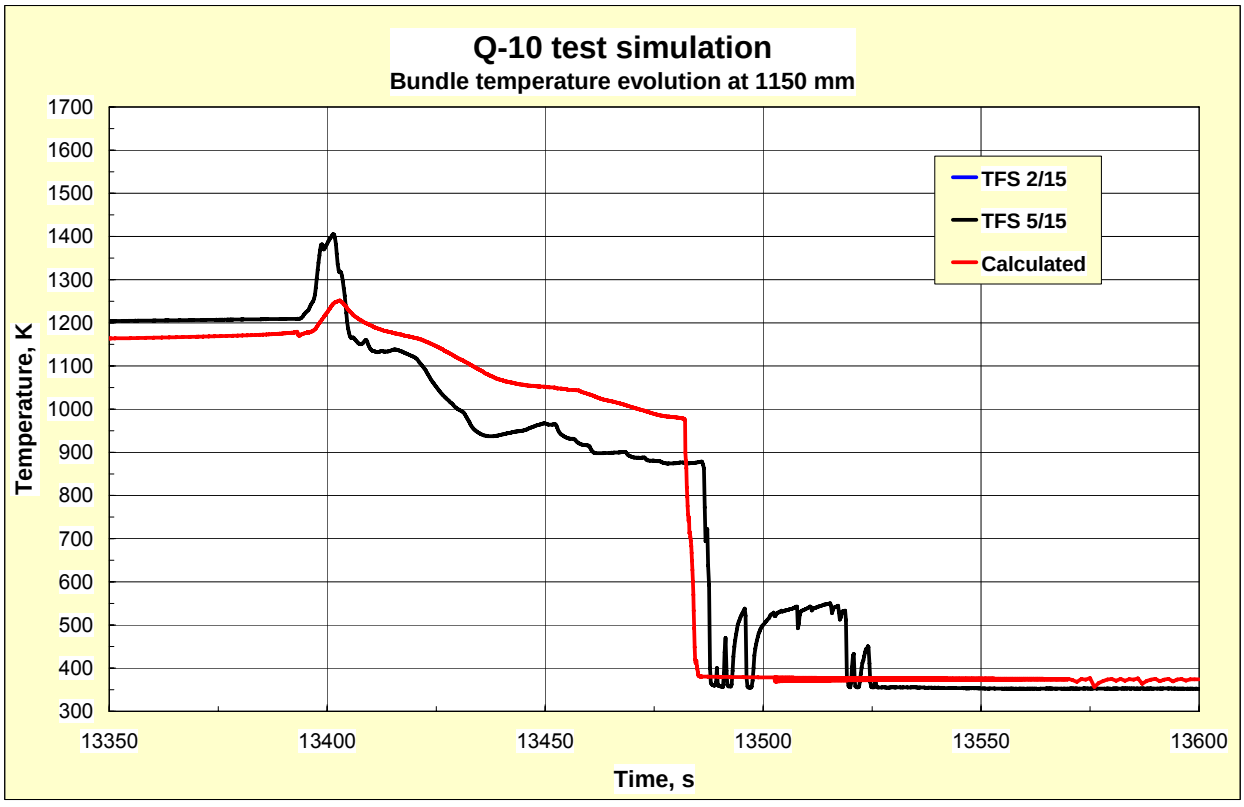

Fig 24. The experimentally measured temperatures at the elevation 1150 mm: TFS2/15 data (blue line) and TFS5/15 data (black line) and calculated temperature evolution of the central rod outer surface (red line). Quenching phase (time period 13350 – 13600 sec.).

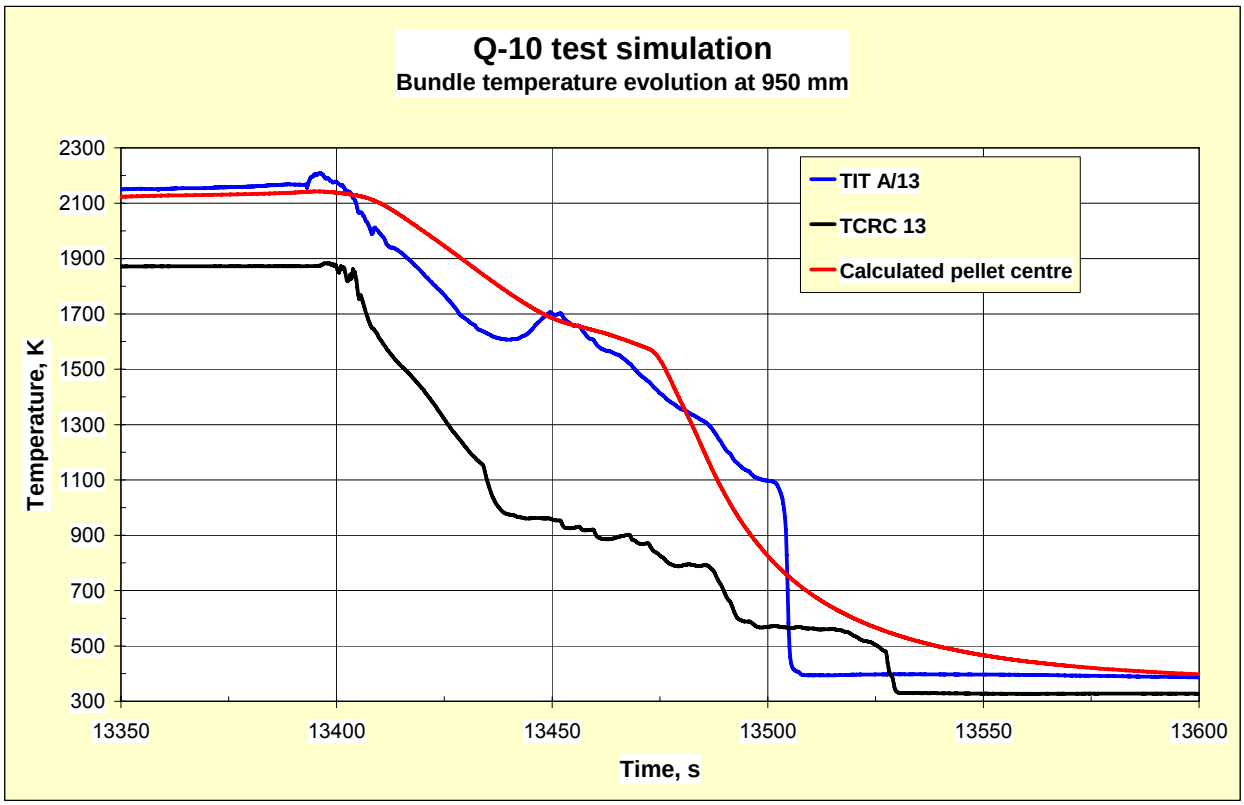

Fig 25. The experimentally measured temperatures at the elevation 950 mm: TIT A/13 data (blue line) and TCRC 13 data (black line) and calculated temperature evolution in the central rod pellet centre (red line). Quenching phase (time period 13350 – 13600 sec.).

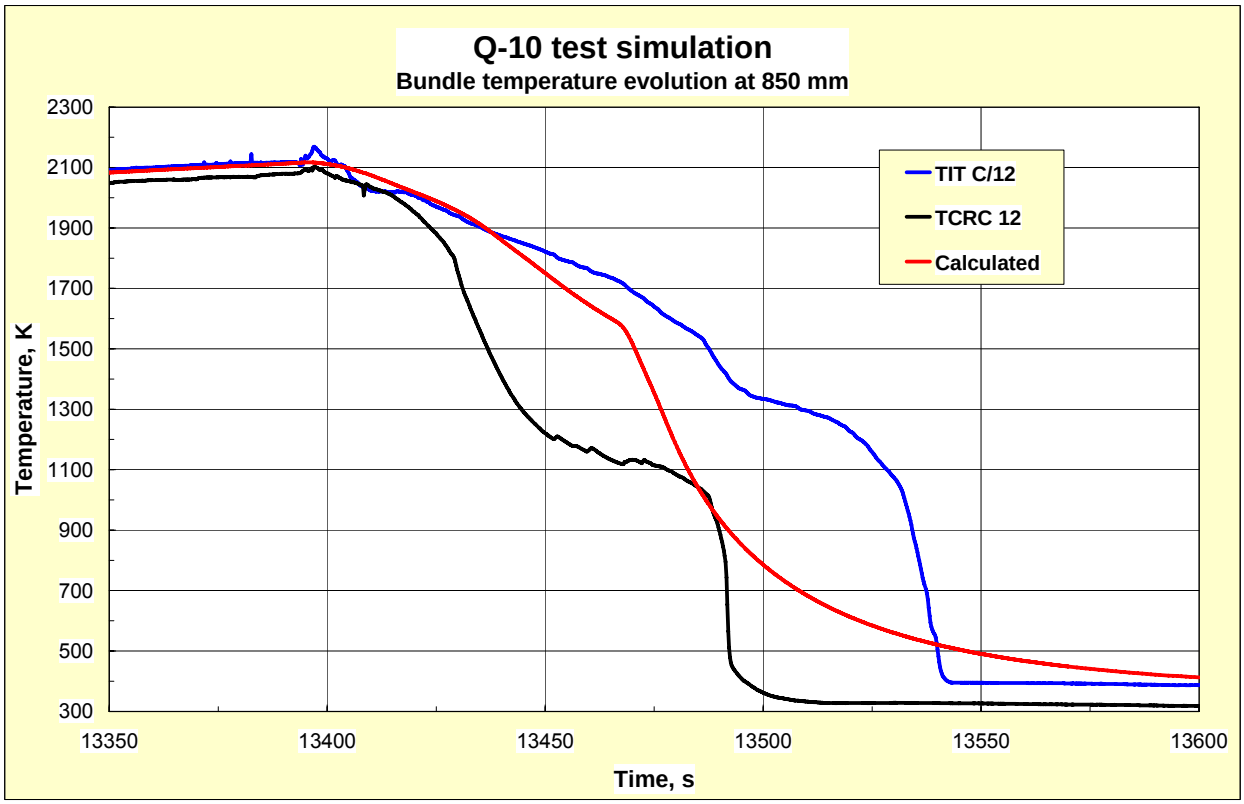

Fig 26. The experimentally measured temperatures at the elevation 850 mm: TIT C/12 data (blue line) and TCRC 12 data (black line) and calculated temperature evolution in the central rod pellet centre (red line). Quenching phase (time period 13350 – 13600 sec.).

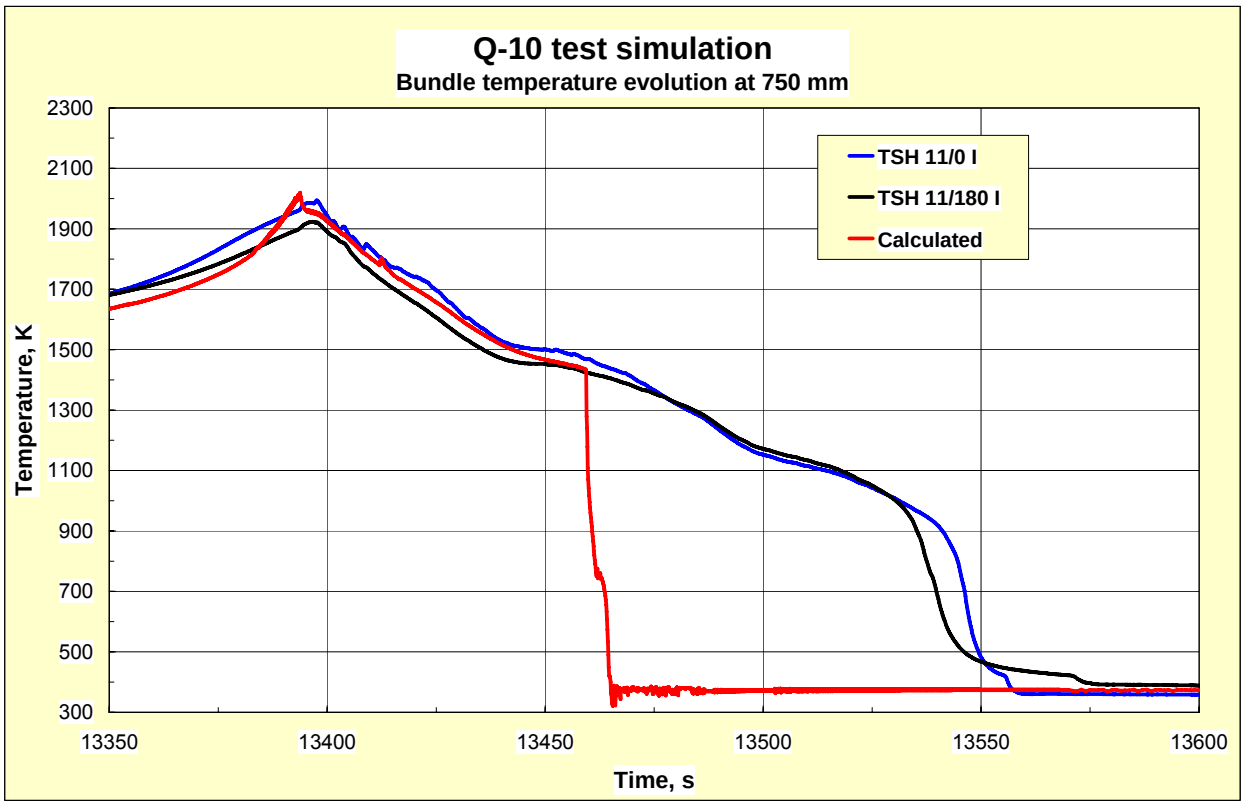

Fig 27. The experimentally measured temperatures at the elevation 750 mm: TSH 11/0_I (blue line), TSH 11/180_I (black line) and calculated temperature evolution of the central rod outer surface (red line).Quenching phase (time period 13350 – 13600 sec.).

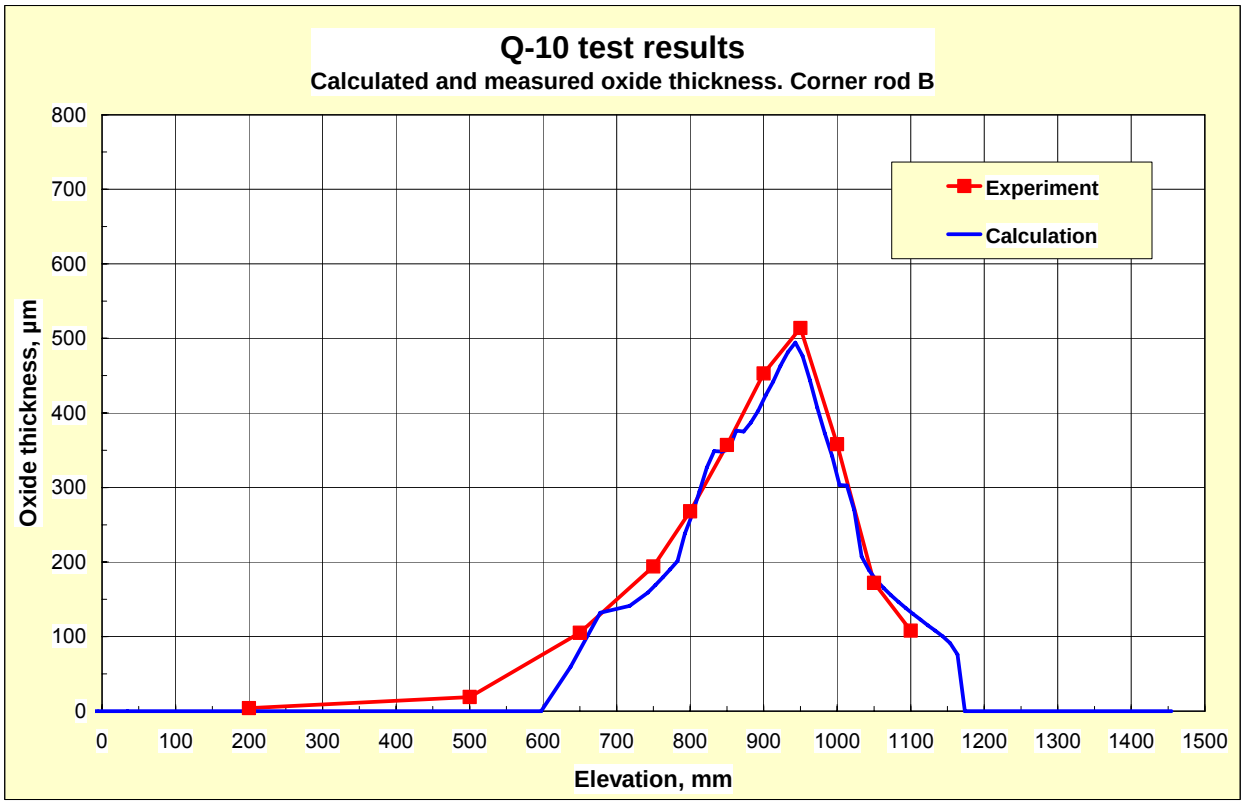

Fig 28. Oxide layer thickness axial profile of corner rod B (withdrawn from the test bundle at 11373 sec.) compared to the calculated one of the central rod for the same time.

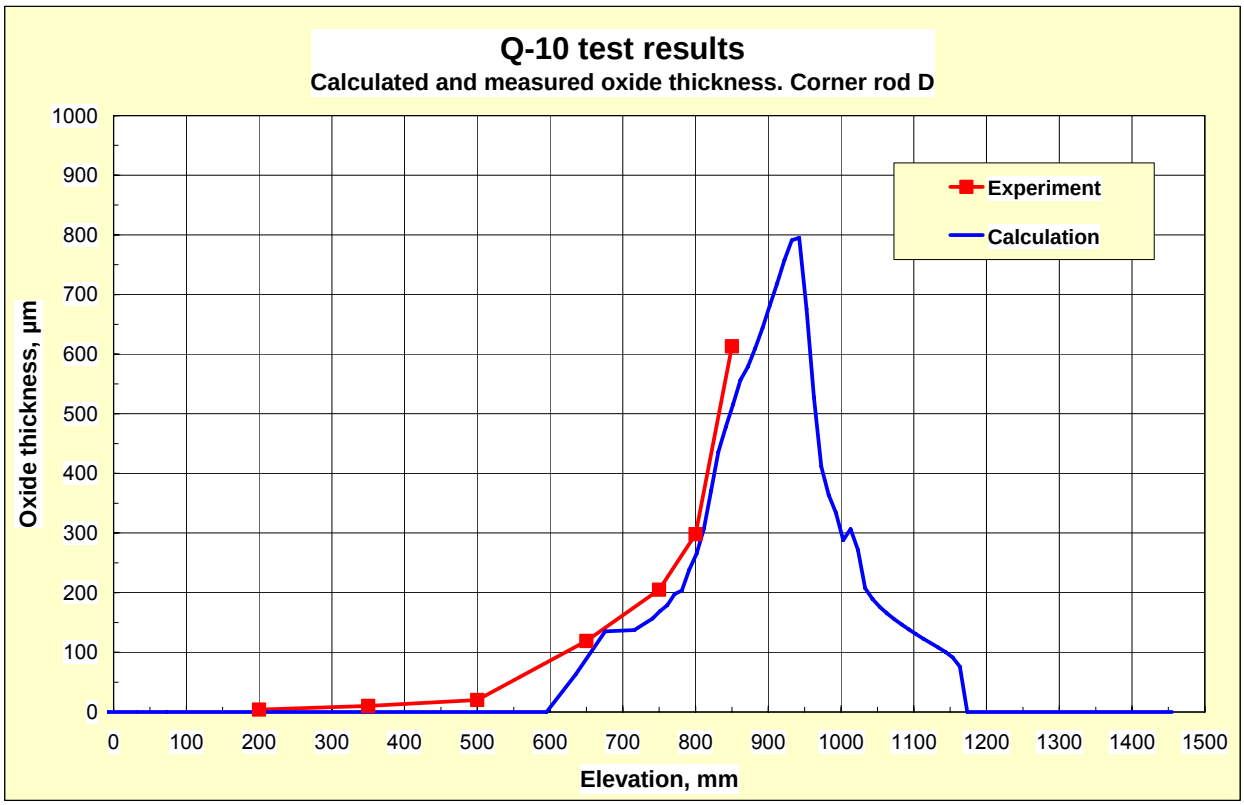

Fig 29. Oxide layer thickness axial profile of corner rod D (withdrawn from the test bundle at 13275 sec.) compared to the calculated one of the central rod for the same time.

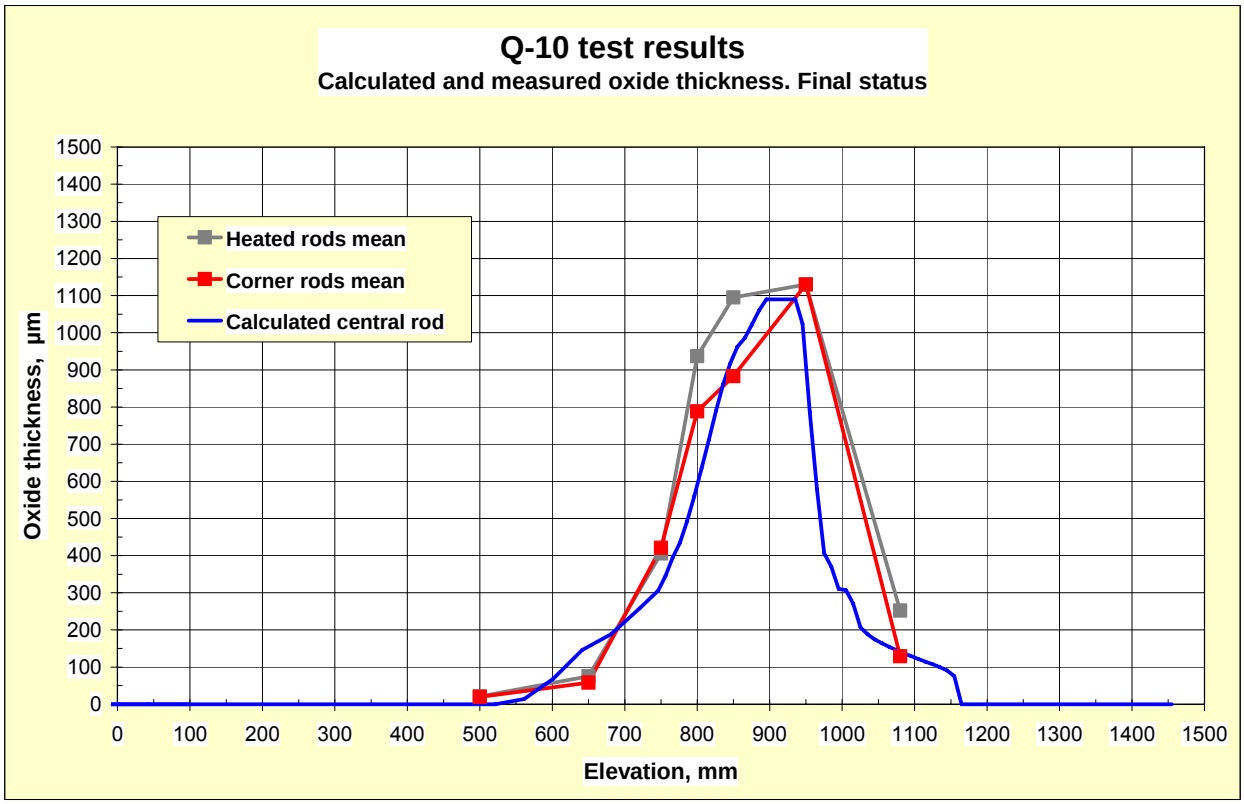

Fig 30. Measured oxide layer thickness profiles of the heated rods (average), and of the corner rods, both at final state, compared to the calculated oxide layer thickness profile of the central rod (final state).

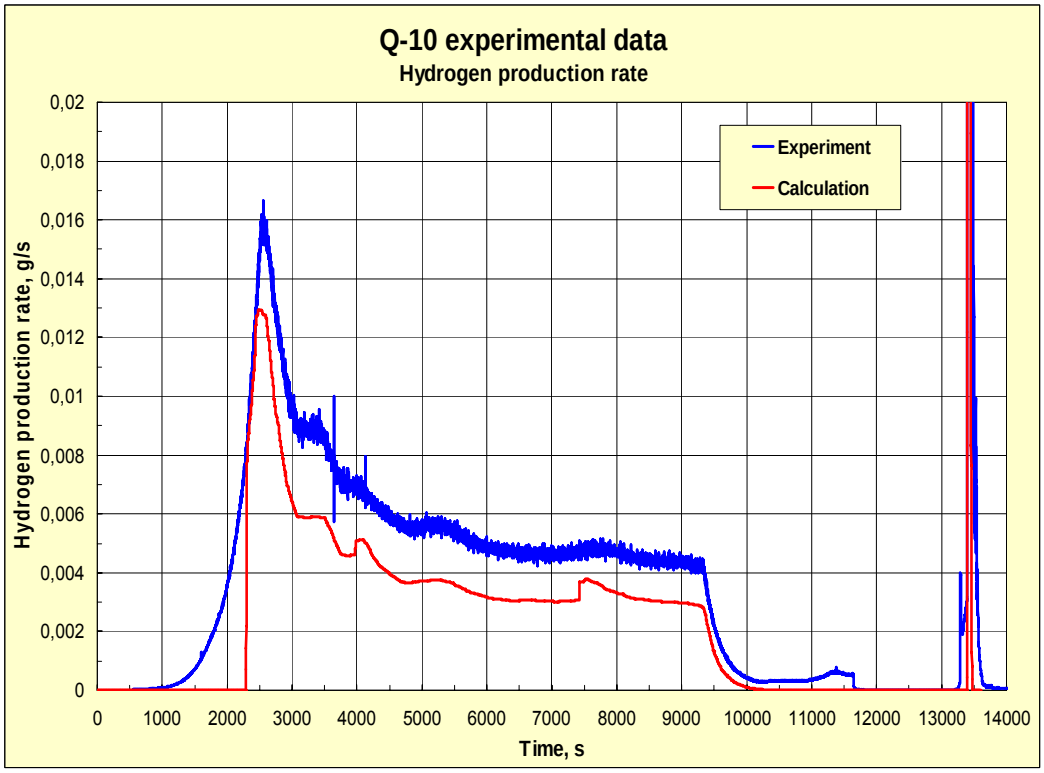

Fig 31. Experimentally measured (blue line) and calculated (red line) hydrogen production rate.

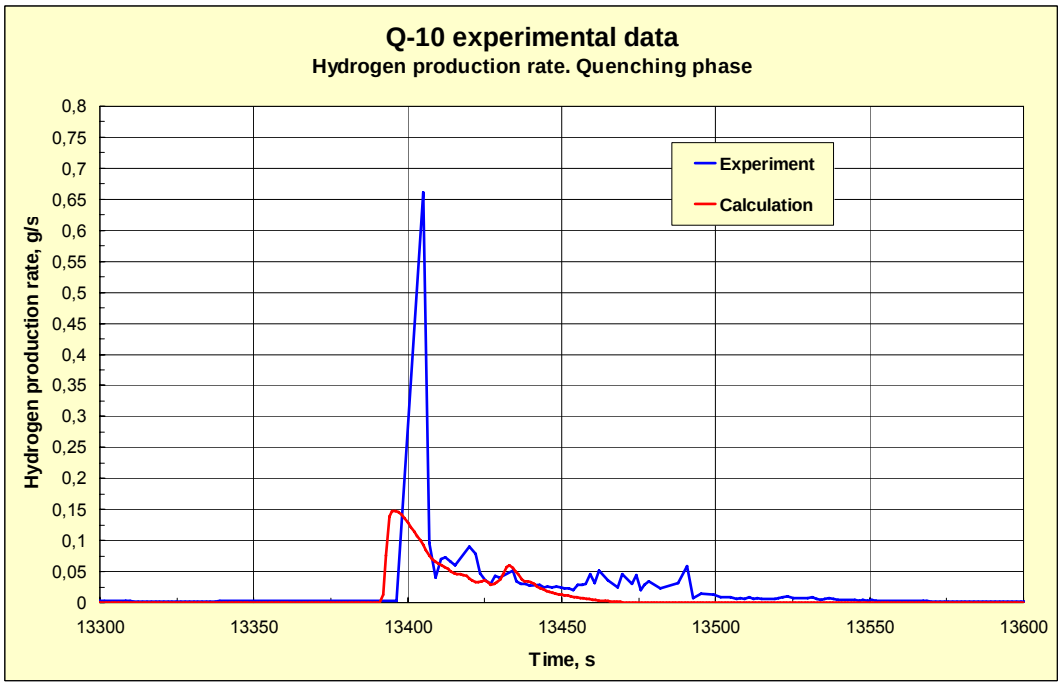

Fig 32. Experimentally measured (blue line) and calculated (red line) hydrogen production rate. Quenching phase (time period 13300 – 13600 sec.)